University of Southern Queensland
Faculty of Health, Engineering & Sciences

3-Dimensional Detached Eddy Simulations of a Novel Variable Geometry Radial Ejector

A dissertation submitted by
Lachlan Rae

in fulfilment of the requirements of
ENP4111 Professional Engineering Research Project

towards the degree of
Bachelor of Engineering (Honours) (Mechanical)

Submitted: November, 2024

Abstract

Ejectors are often described as compressors with no moving parts, a low maintenance and reliable device capable of being powered by sustainable energy. Their greatest downfall, however, is their low efficiency which is often attributed to their performance being a function of both operating conditions and geometry. For fixed geometry ejectors great care needs to be taken to keep the flow pressures at a constant value. As an alternative to this much work has been done to provide solutions based on variable geometries. The traditional axial ejector configuration makes this process difficult without impeding of the flow through the ejector. Instead a novel solution has been developed in the form of the variable geometry radial ejector (VGRE).

From its initial inception to the present, the VGRE has shown promising results compared to axial ejectors in both numerical and experimental investigations. The purpose of the present work is to develop a 3-dimensional (3D) detached eddy simulation (DES) model to assist in further development of the device in a cost effective manner. The intended application for the VGRE is for use in solar-powered ejector refrigeration systems. The development of this device will increase the capability and efficiency of the sustainable cooling technology. The ability to reliably assess the VGRE by numerical methods is paramount to its development, this is the reasoning behind the present work.

A full review of the improved VGRE's development to date was conducted to gain a full understanding of the device and the requirements needed for a suitable simulation model. Additional research was conducted into the literature regarding ejector refrigeration systems, ejector performance metrics, and ejector geometry. During this process relevant data was obtained for creating geometries and performing computational fluid dynamic (CFD) analyses. Previously documented experimental data was also collected for the purpose of validating the CFD model.

Previous studies had conducted 2D axisymmetric simulations and determined the optimal DES turbulence model for the improved VGRE to be the DES Realizable k-ϵ model. Replication of the 2D simulations was performed as a means to familiarise the author with the CFD analysis methods and program, ANSYS Fluent. Nine geometries and meshes were reproduced to represent different configurations of the adjustable VGRE. Several simulations were performed resulting in very poorly agreeing solutions. Difficulties identifying the issue lead to a sample simulation being acquired from a previous study for comparison. Other than minor geometry and mesh variances there were no

issues identified. A number of subsequent simulations were conducted in an attempt to determine the problem, but to no avail. Project time constraints required the 2D simulations be concluded and work continued with the 3D simulations.

The acquired 2D geometry was adapted into a 3D model and several meshing methods were tested. The meshing process was hindered by insufficient hardware resulting in long mesh processing times. Eventually, a relatively simple mesh was utilised to simulate the improved VGRE. Unfortunately the simulation provided very poor agreement to the experimental data. Although, a certain level of agreement was noticed between the 3D and 2D simulations conducted in the present work.

The cause of the poor simulations could not be ascertained and as such the project was deemed a failed process. Upon preparing this dissertation, however, a previously unknown parameter was identified relating to pressure settings. By default, this setting had introduced a gross error into the simulations causing the poor simulations. By this point, however, there was insufficient time to perform any more simulations.

This dissertation discusses the efforts undertaken, albeit unsuccessful, to develop a reliable 3D DES model for the simulating the improved VGRE.

University of Southern Queensland

School of Engineering

ENP4111 Research Project

Limitations of Use

The Council of the University of Southern Queensland, its School of Engineering, and the staff of the University of Southern Queensland, do not accept any responsibility for the truth, accuracy or completeness of material contained within or associated with this dissertation.

Persons using all or any part of this material do so at their own risk, and not at the risk of the Council of the University of Southern Queensland, its School of Engineering or the staff of the University of Southern Queensland.

This dissertation reports an educational exercise and has no purpose or validity beyond this exercise. The sole purpose of the course pair entitled “Research Project” is to contribute to the overall education within the student’s chosen degree program. This document, the associated hardware, software, drawings, and other material set out in the associated appendices should not be used for any other purpose: if they are so used, it is entirely at the risk of the user.

University of Southern Queensland

Faculty of Health, Engineering and Sciences

ENG4111/ENG4112 Research Project

Certification of Dissertation

I certify that the ideas, designs and experimental work, results, analyses and conclusions set out in this dissertation are entirely my own effort, except where otherwise indicated and acknowledged.

I further certify that the work is original and has not been previously submitted for assessment in any other course or institution, except where specifically stated.

Lachlan Rae

[redacted]

Acknowledgments

First of all I would like to acknowledge and thank my supervisor, Dr Khalid Saleh, not only for his assistance and guidance throughout the course of this project, but also for his support outside of the project throughout the year. In spite of all the difficulties presented during this project you help make it an enjoyable and educational experience.

I would also like to thank my peers for providing the environment to bounce ideas off each other, and giving the extra perspective to help solve the issues. It was reassuring to know we were all in it together.

Finally, to my family and friends who kept me going through it all, especially my wife and daughter, who's support urged me on when I needed it most. Thank you all for the love and support.

Lachlan Rae

Contents

List of Figures

List of Tables

Nomenclature

ω	Entrainment ratio
$\dot{m}_p$	Primary mass flow rate in kg/s
$\dot{m}_s$	Secondary mass flow rate in kg/s
r_e	Expansion ratio
P_p	Primary pressure in kPa
P_s	Secondary pressure in kPa
r_c^*	Critical compression ratio
P_o^*	Critical outlet pressure
COP	Coefficient of performance
Q_e	Thermal energy removed by the evaporator in kW
Q_g	Total energy introduce to the system by the generator in kW
W_{in}	Mechanical work in kJ
CC	Cooling capacity in kW
$h_{e,out}$	Specific enthalpy at outlet of evaporator in kJ/kg
$h_{e,in}$	Specific enthalpy at inlet of evaporator in kJ/kg
COP_{SoERS}	Coefficient of performance for a solar-powered ejector refrigeration system
η_{sc}	Efficiency of solar collector
η	Isentropic efficiency
γ	Ratio of specifics heats
T	Temperature in K
d	Nozzle throat separation in mm
D	Duct throat separation in mm

Glossary Of Terms

CFD	Computation Fluid Dynamics
VGRE	Variable Geometry Radial Ejector
3D	3-Dimensional
DES	Detached Eddy Simulation
2D	2-Dimensional
ERS	Ejector Refrigeration System
SERS	Single Ejector Refrigeration System
COP	Coefficient Of Performance
CC	Cooling Capacity
SoERS	Solar-powered Ejector Refrigeration System
NXP	Nozzle eXit Position
AR	Area Ratio
PLC	Programmable Logic Controller
RANS	Reynolds Averaged Navier-Stokes
PT	Pressure Transducer
FMD	Flow Meter Device
TC	Thermocouple
Ba	Barometer
HPC	High Performance Computer
AR_n	Nozzle Area Ratio

Chapter 1

Introduction

1.1 Outline of Project

The focus of this project is to develop a suitable 3-dimensional (3D) model for simulating a novel variable geometry radial ejector (VGRE) for use in ejector refrigerator systems that utilise low grade thermal energy such as solar power. These systems are often susceptible to poor efficiency as a result of transient thermal input varying the operating conditions. For fixed geometry ejectors, this is problematic, as their optimal operating conditions are restricted to a small range. To mitigate this issue the VGRE has been designed with the ability to provide multiple degrees of geometric adjustment whilst not impeding on the fluid flow. Implementation of a feedback control system to the ejector's adjustable features could allow for optimal efficiency over an increased range of operating conditions. This is a significant advantage over existing ejector technology and promotes the adoption of sustainable solar energy use for cooling applications. Although the VGRE is still in early stages of development, it has provided promising results already compared to existing axial technology. By developing an accurate simulation model for this device, further research can be performed for the technology in a cost effective and safe manner.

1.2 Aims and Objectives

The aim of this project is to develop a cost effective computational fluid dynamics (CFD) model for a novel VGRE using a 3D detached eddy simulation (DES) method. Experimental and numerical analyses of the device have previously been performed to develop the VGRE to a promising level of efficiency compared to existing ejector technology. To continue the development and improve this efficiency further it is essential that a reliable numerical model is ascertained. Several objectives were identified as being key milestones for meeting this aim:

- **Research**

  Conduct an extensive review of Rahimi's (2017) and Al-Rbaihat's (2020) theses as well as any literature pertaining to the development of the improved VGRE to ensure the development of the device is performed with a full understanding of its background, current operating capabilities, and any potential future developments.

- **2-Dimensional (2D) Analyses**

  Replicate the 2D CFD simulations performed by Al-Rbaihat (2020) and verify the results against the original simulations to provide understanding of the numerical processes that are required for analysing the improved VGRE.

- **3D Model Development**

  Develop a 3D geometry model of the improved VGRE and establish a suitable mesh for conducting 3D DES simulations.

- **3D Analyses**

  Perform 3D simulations of the improved VGRE for a range of operating conditions and geometric configurations.

- **Data Analysis**

  Compare the results of the 2D and 3D simulations, and validate using the experimental data from Al-Rbaihat (2020) to determine the accuracy of the modelling.

- **Reporting and Presentation**

  Prepare a full report of the project outcomes and present the findings to a group of engineering peers.

1.3 Dissertation Overview

Chapter 2: Literature Review

This chapter reviews several factors pertaining to the improved VGRE. Beginning with typical applications for ejectors and expanding on ejector refrigeration systems. Ejector performance metrics are discussed which leads to the effects that geometry have on performance. An extensive review of Rahimi (2017) is conducted regarding his work designing and developing the original VGRE

prototype. The chapter concludes with another extensive review of the work by Al-Rbaihat (2020) which investigates and develops the improved VGRE based on the work presented by Rahimi (2017).

Chapter 3: 2D Simulations

The process of replicating the geometry and mesh from Al-Rbaihat (2020) is discussed. This includes variations in the produced geometries and a mesh quality comparison. Multiple simulations are performed using several versions of ANSYS Fluent and the results are compared for further development considerations.

Chapter 4: 3D Simulations

Development of the 3D geometry and mesh is performed resulting in several potential variations. These models are assessed against each other and a choice is made for use in the initial 3D simulations. The simulations are performed and the solutions are compared and discussed.

Chapter 5: Conclusion

A summary of the work performed is provided with a discussion of any insights gained throughout the project. The presented work is concluded with recommendations of future development options for the improved VGRE.

Chapter 2

Literature review

2.1 Chapter Overview

The following chapter presents a review of the literature, investigating relevant studies that offer insight into the work of this dissertation. The discussion touches on general applications for ejectors, before expanding on their use in solar-powered ejector refrigeration systems. The performance metrics of ejectors is described and also the relationship between certain geometrical features of the device and their performance. Finally, an extensive review of Rahimi's (2017) thesis - 'Investigation of Radial Flow Ejector Performance Through Experiments and Computational Simulations', and Al-Rbaihat's (2020) thesis - 'Design of Variable Geometry Radial Ejector for HVAC Purposes Through Experiments And Simulation', is performed to gain a full understanding of the development of the variable geometry radial ejector from inception to present.

2.2 Introduction

An ejector is a device that is often described as a compressor with no moving parts, it utilises a primary high pressure or motive fluid passing through a converging-diverging (supersonic flow) nozzle to entrain and compress a secondary low pressure or entrained fluid in a co-flow configuration. As the high pressure fluid passes through the nozzle its pressure is decreased and velocity is increased drawing in the low pressure fluid for mixing. The entrained fluids then pass through a diffuser decreasing the velocity and increasing the pressure, resulting in an overall pressure increase for the secondary fluid. (Elbel & Lawrence 2016).

Initially invented in 1858 by Henri Giffard, the ejector was designed as a replacement for mechanical pumps used to circulate water back to the reservoir in steam engines boilers. This design was later improved by Schau with the implementation of a converging-diverging nozzle in 1869 (Elbel &

Hrnjak 2008). Since then numerous applications and developments have been investigated for ejectors. Industrial processes such as polymerisation and crystallisation (Yadav, Pandey, & Gupta, 2021), fluid mixing and agitation of liquids and slurries (Darweesh 2024), and vacuum generation for manufacturing (Niu & Zhang 2024) , have all been discussed recently in the literature. Liu et al. (2019) investigated ejector use for desalination applications, nuclear reactor safety protocols use ejectors to pump emergency cooling water, as reported by Beithou and Aybar (2000), and the aerospace industry have employed the technology in rocket engines (Shi et al. 2019). One of the highly utilised and studied applications for ejector technology, and the most pertinent to the work of this paper, is its use in refrigeration and air conditioning systems.

2.3 Ejector Refrigeration Systems

A comprehensive review of ejector refrigeration technologies was performed by Besagni, Mereu, and Inzoli (2016) and identified 8 different ejector refrigeration systems (ERS) with multiple variants of each, that have been studied in the literature, Figure 2.1 shows an overview of the these systems. Whist the design of the radial geometry ejector has been found to have the potential for increased performance over traditional axial designs and could benefit any of these refrigeration systems, it has been expressed that the initial focus for the technology is to assist in the performance of solar or low grade powered ejector refrigeration systems (Rahimi 2017; Al-Rbaihat 2020).

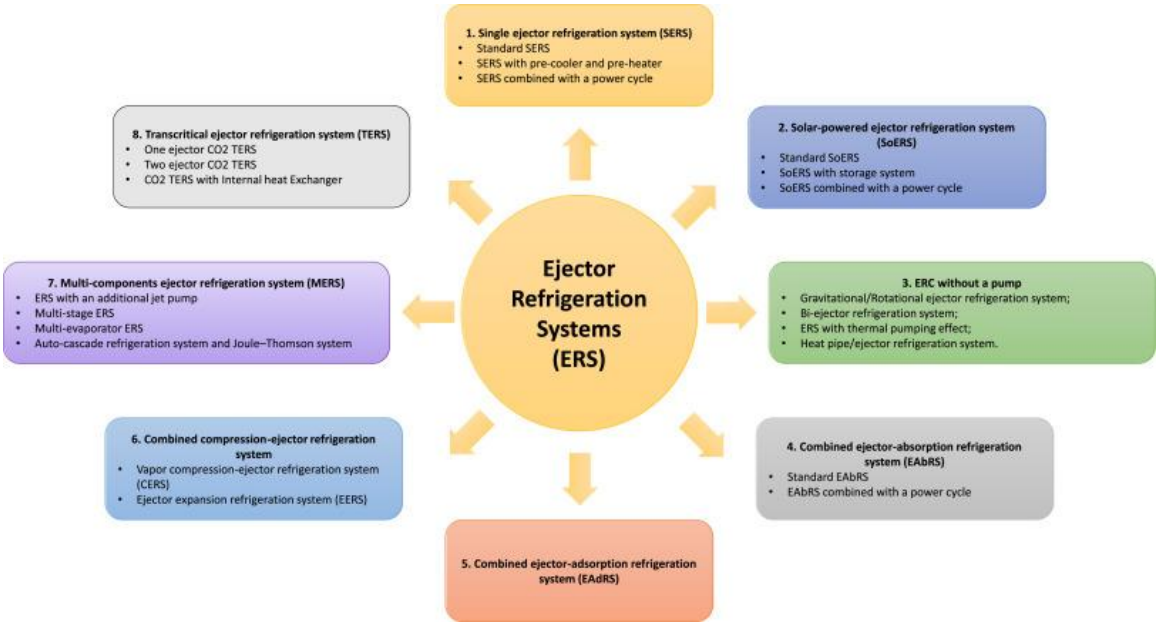

Figure 2.1: Overview of ejector refrigeration systems (Besagni, Mereu & Inzoli 2016).

The single ejector refrigeration system (SERS) is the most basic form of the ejector refrigeration systems and consists of a generator, evaporator, condenser, throttling valve, pump, and ejector. The generator processes the working fluid into a vapour by adding low-grade heat energy to it. Once saturation conditions are achieved, the high pressure (primary) flow is delivered to the ejector nozzle increasing the flow velocity and entraining the low pressure (secondary) vapour flow received from the evaporator. The mixed flows are recompressed elevating the pressure of the secondary flow before continuing to the condenser where heat flux is rejected to the environment through a condensation process. From here the liquid flow is divided in two, with one part being expanded isenthalpically through the throttling valve and sent to the evaporator providing the system's cooling effect, and the other part being pumped back to the generator to continue the cycle. One main feature of this system is the ability to set operating conditions for the generator and evaporator to allow the ejector to operate at critical conditions and provide a constant coefficient of performance (COP) and cooling capacity (CC) (Besagni, Mereu & Inzoli 2016). By introducing a solar collector into the SERS a new refrigeration system is portrayed, the solar-powered ejector refrigeration system (SoERS) (figure 2.2). Here the solar collector, often flat plate or evacuated tube (Bellos and Tzivanidis 2017), is used to heat an intermediate fluid which is pumped to the vapour generator for process heat (Besagni, Mereu & Inzoli 2016).

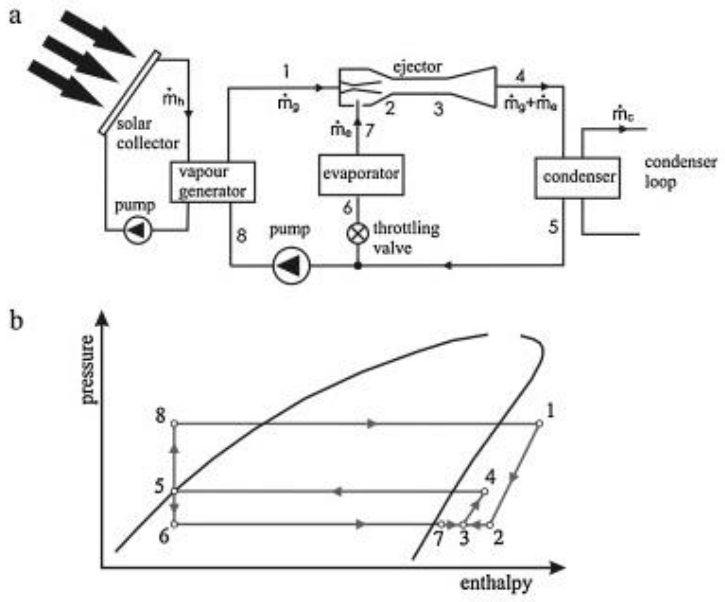

Figure 2.2: Schematic and P/h diagram of a solar-powered ejector refrigeration system (Śmierciew et al. 2014).

Numerous studies have been conducted on various solar-powered ejector refrigeration systems investigating the effects of different refrigerants on their performance. R141b was tested by Huang et al. (1998 and 2001), Vidal et al. (2006), Colle et al. (2009), Dennis and Garzoli (2011), and Bellos and Tzivanidis (2017), with system COP's ranging from 0.12 to 0.25. Korres et al. (1989) and Sokolov and Hershgal (1993) attained COP's between 0.08 and 0.35 using R114. Investigations into the use of R600a by Pridasawas and Lundqvist (2007), Chesi et al. (2013), and Śmierciew et al. (2014) returned COP's ranging from approximately 0.04 to 0.23. One of the more investigated system types utilised steam ejectors with studies by Nguyen et al. (2001), Khattab and Barakat (2002), Pollerberg et al. (2008 and 2009), Varga et al. (2009), Allouche et al. (2012), Diaconu (2012), Ali (2013), and Joemann et al. (2016) producing COP's ranging between 0.1 and 0.57. These values provide an understanding of the typical performance achieved by solar-powered ejector refrigeration systems and help to identify a benchmark for the efficiency of the improved VGRE. It should be noted, however, that some of the investigations utilised addition hardware such as booster compressors and auxiliary heaters in the configuration of their systems and should be consider when making comparisons to the improved VGRE.

2.4 Ejector Performance Metrics

Whilst the performance of SoERS' can be attributed to by the ejector, the performance of the ejector itself is assessed independently. The performance of an ejector is most commonly attributed to two factors, its entrainment ratio and its critical outlet pressure, also known as critical back pressure. The entrainment ratio (ω) is defined as the ratio of the mass flow rate of the secondary flow ($\dot{m}_s$) to the mass flow rate of the primary flow ($\dot{m}_p$).

$$\omega = \frac{\dot{m}_s}{\dot{m}_p} \tag{2.1}$$

The critical outlet pressure is determined to be the pressure where the entrainment ratio starts to decrease as the outlet pressure is increased further (Al-Rbaihat 2020). These factors are influenced by both the operating conditions and the geometry of the ejector.

For a fixed geometry ejector, the geometry usually depends on specific operating conditions for optimal efficiency. The operating conditions can be described using the expansion ratio (r_e), defined as the ratio of primary pressure ($\mathrm{P_p}$) to secondary pressure ($\mathrm{P_s}$) , and the critical compression ratio ($\mathrm{r_c^*}$), defined as the ratio of the critical outlet pressure ($\mathrm{P^*_o}$) of the ejector to the secondary pressure

(Rahimi 2017). The critical outlet pressure is defined as the outlet pressure where the entrainment ratio starts to decrease, as the outlet pressure is increased.

$$r_e = \frac{P_p}{P_s} \tag{2.2}$$

$$r_c^* = \frac{P^*_o}{P_s} \tag{2.3}$$

Additional performance metrics for ejector refrigeration systems as a whole include the coefficient of performance (COP), defined as the ratio of thermal energy removed by the evaporator (Q_e) to the thermal energy introduce to the system by the generator (Q_g) plus any mechanical work done (W_{in}), and the cooling capacity (CC), defined as the mass flow rate of the secondary fluid multiplied by the change in specific enthalpy of the refrigerant caused by the evaporator ($h_{e,out}$ - $h_{e,in}$) (Besagni, Mereu & Inzoli 2016). It should also be noted that the performance of the SoERS (COP_{SoERS}) is not only calculated by the COP of the system but also the efficiency of the solar collector (η_{SC}) (Huang et al. 1998).

$$COP = \frac{Q_e}{Q_g + W_{in}} \tag{2.4}$$

$$CC = \dot{m}_s\left(h_{e,out} - h_{e,in}\right) \tag{2.5}$$

$$COP_{\text{SoERS}} = COP \times \eta_{SC} \tag{2.6}$$

One final metric for the performance of an ejector is its isentropic efficiency (η), which can be defined as the work required to compress the secondary fluid divided by the work required to expand the primary fluid. For an ideal gas the isentropic efficiency of an ejector can be calculated from (2.7).

$$\eta = \omega \times \frac{\left(P_o/P_s\right)^{\frac{\gamma-1}{\gamma}} - 1}{1 - \left(P_o/P_p\right)^{\frac{\gamma-1}{\gamma}}} \tag{2.7}$$

Where 'γ' is the specific heat ratio. The isentropic efficiency can be considered a comprehensive performance indicator as it is a function of the primary, secondary, and outlet pressures, as well as the primary and secondary mass flow rates (Al-Rbaihat 2020). From (2.7) it can be determined that

the optimal efficiency is calculated when the entrainment ratio and critical outlet pressure are at their maximum values for the given operating conditions.

Whilst these metrics rely primarily on the operating conditions of the system to determine the ejector's performance, the geometry of the ejector also plays a major role as it ultimately determines the outlet pressure of the ejector, effecting the critical compression ratio and the isentropic efficiency calculations for the device.

2.5 Ejector Geometry

As previously mentioned the geometry of an ejector is a major factor in its efficiency and dictates the performance of the device when the operating conditions are not steady, such as those present in systems that utilise solar power. This is because for any fixed ejector geometry there is only a small range of primary and secondary pressures that provide critical operating conditions, i.e. when the ejector is at its most efficient. Many geometric features and relationships have been investigated in the literature as a means to increase the understanding of the flow behaviours and improve the efficiency of ejectors. Primary nozzle geometry and positioning, area ratios, and suction chamber geometry are some of the more studied parameters. Figure 2.3 depicts the sections of a typical axial ejector.

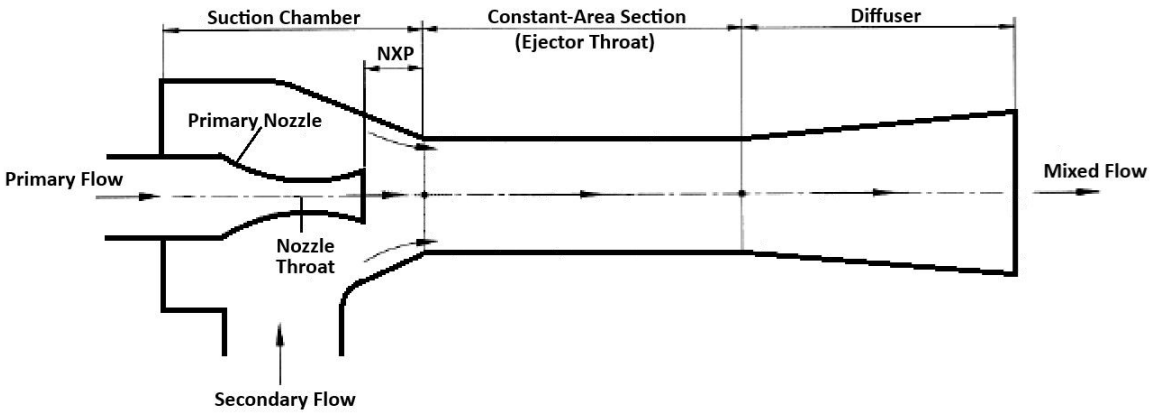

Figure 2.3: Diagram of axial ejector sections.

Many studies have been conducted with respect to primary nozzle geometries, namely the nozzle exit position (NXP). The NXP is defined as the distance from the primary nozzle exit to the entrance of the constant area section (ejector throat) (Rand et al. 2022). Chong et al. (2014) determined that there is an optimal NXP that corresponds to the maximum entrainment ratio and Kumar et al. (2019) also noted that the entrainment ratio was very sensitive to the NXP. Furthermore, Poirier (2022) investigated a dimensionless NXP value by dividing the NXP by the diameter of the constant area section, and in doing so determined that the operating pressures had zero effect on this value. The NXP may be a useful geometric parameter for improving the VGRE if these relationships transfer to a radial configuration, further consideration should be considered.

Area ratios are used to compare different ejectors that would otherwise be too difficult to compare. The ejector area ratio (AR) is the ratio of the ejector throat area to the nozzle throat area. This geometric relationship has been shown to have an effect on the entrainment ratio of an ejector as well as the primary and secondary flow pressures. Lui et al. (2017) noted the AR had a direct relationship to the entrainment ratio, but an inverse relationship to the critical back pressure. Jia and Wenjian (2012) made several observations regarding AR including, maximum cooling capacities and COPs can be achieved with optimum AR; cooling capacities are related to both AR and nozzle diameter whilst COPs are only dependent on the AR; and the optimum AR has a linear relationship to the primary pressure, this last observation was also noted by Wang et al. (2018). Yu, Zou, and Yu (2024) also identified a relationship whereby the optimal AR increased as the length of the constant-area ejector throat section increased. Understanding these relationships that the AR has with the function and performance of ejectors is a key concept for the development of the improved VGRE.

The suction chamber, or mixing section converging, angle has been studied for a range of operating conditions and working fluids with varied results. The following angles were all determined to be the optimum values for their respective studies:

- 0.5° (Utomo et al. 2008)
- 1.45° - 4.2° (Zhu et al. 2009)
- 28° (Chong et al. 2009)
- 1° (Ji et al. 2010)
- 6° (Kouhikamali & Sharifi 2012)
- 6° - 8° (Lin et al. 2013)
- 12° (Ramesh & Sekhar 2018)

These mixing section converging angles were defined as the optimum values for promoting the maximum entrainment ratio for each of their respective scenarios. Whilst these studies were all based on axial flow ejectors, the relationship may not directly apply to the design of the improved VGRE. However, a potential correlation may exist between the geometry of the secondary flow path entrance of the radial design and the mixing section converging angle as studied above.

To gain a full understanding of the VGRE and its geometric features it is best to examine the design beginning with its inception. A review of Rahimi's (2017) thesis will provide this insight in the next section.

2.6 Original VGRE

2.6.1 Introduction

The concept of a variable geometry radial ejector was first expressed by Ng and Otis in 1979 but has been relatively unexplored since, with the exception of CFD analyses performed by Ababneh et al. in 2009 in which an arrangement of eight rotary nozzles with a radial diffuser were conceived. In 2017, Hadi Rahimi submitted his thesis entitled 'Investigation of Radial Flow Ejector Performance Through Experiments and Computational Simulations', this work marks the inception of the device that this current dissertation ultimately represents. This concept posited the concept of an axial flow ejector transformed into a radial arrangement, giving it comparable geometric characteristics allowing for the use of an existing physical axial flow ejector as a reference point for operational comparison. The following sections review Rahimi's (2017) work with respect to the methodology presented in his thesis.

2.6.2 Investigation of Radial Flow Ejector Concept through CFD Analysis

Established axial flow ejector design procedures were employed where possible to produce a radial flow model that matched the geometric characteristics and performance of a predetermined axial flow ejector design. However, it should be noted that these procedures could only be loosely followed due to the comparative complexity of the radial flow path as shown in figure 2.4. Table 2.1 outlines the geometric characteristics of the radial design with respect to its axial counterpart. The most notable difference in these parameters is the divergent part length, this is a fortunate consequence of the radial configuration which allows for a similar AR in a physically smaller device.

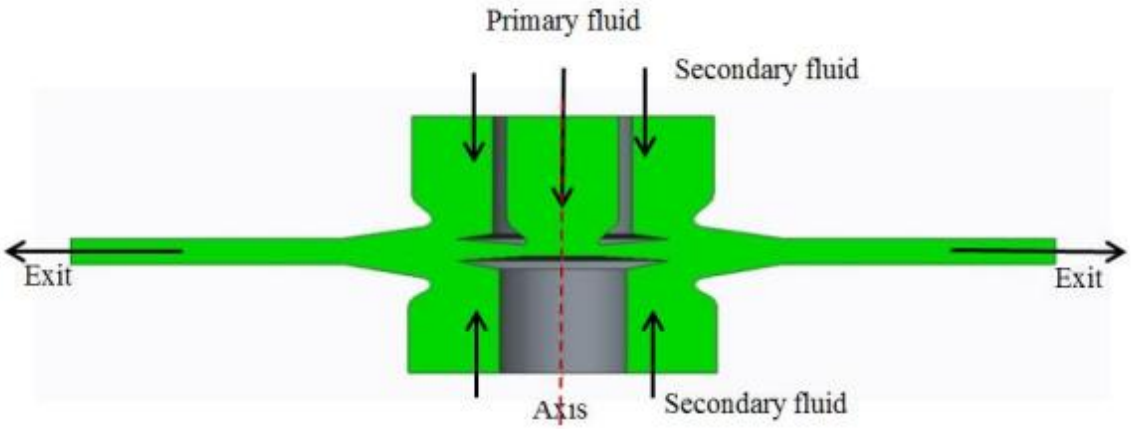

Figure 2.4: Diagram of radial ejector flow paths.

Table 2.1: Equivalent geometric characteristics of radial and axial flow ejectors with respect to ejector AR.

Characteristic	Radial Flow	Axial Flow
Nozzle throat area (mm^2)	8.792	8.54
Nozzle exit area (mm^2)	179	154
Nozzle area ratio	20	18
Divergent part length (mm)	9.5	59.5
Divergent half angle	5°	5°
Ejector throat area (mm^2)	498	506
Ejector area ratio	58.24	59
Ejector convergent half angle	9°	10°
Ejector divergent half angle	0°	3.5°

The use of an already existing axial flow model also provided a mesh independence study and experimentally validated CFD simulation data (Al-Doori 2013) for comparison with the radial flow case. Meshes consisting of 19832 elements for the axial flow model and 51451 elements for the radial flow model were determined to perform to a sufficient and comparable accuracy, the increased element count for the radial device was due to the relative complexity of its geometry. ANSYS Fluent 14.5 was used to perform simulations on the radial flow model, table 2.2 outlines the parameters used in these simulations.

Table 2.2: Simulation parameters for radial flow model.

Solver Type	Density -Based
2D-Space	Axisymmetric
Time	Steady State
Turbulence Model	RANS k-ω SST
Material	Air as an Ideal Gas
Primary Inlet Boundary Type	Pressure Inlet
Secondary Inlet Boundary Type	Pressure Inlet
Outlet Boundary Type	Pressure Outlet
Formulation	Implicit
Discretisation	Second Order Upwind
Residuals	10^{-5}
Primary Flow Pressure	160, 200, and 250 kPa
Secondary Flow Pressure	1.8, 2.5, and 3.2 kPa
Outlet Pressure	2 to 7 kPa

A series of simulations were conducted using various combinations of primary inlet pressure, secondary inlet pressure, and outlet pressure values. Rahimi concluded that the simulations showed at lower primary pressures the axial ejector performed slightly better than the radial ejector, at high primary pressures the two ejectors performed comparably, and for some operating conditions the radial configuration even outperformed the axial one. It was deemed that the radial simulations were of adequate accuracy, and in providing similar results to the axial model, represented real flow and warranted further investigation into the device.

2.6.3 CFD Study of a Variable Flow Geometry Radial Ejector

The purpose of the new design is to provide multiple degrees of geometric adjustment and as such simulations were performed to test the proof of concept for one of these parameters, the duct throat separation distance. Three 2D-axisymmetric models were created for the analysis with duct separations of 2.2, 2.4, and 3.0 mm. Meshes for the models were created with respect to a mesh independence test from previous work (Rahimi, Malpress & Buttsworth 2016) with element counts of 51451, 53126, and 59324 respectively. All other simulation parameters were the same as the previous simulation as outlined in table 2.2 above.

A series of simulations was run for each of the three models using different combinations of operating pressures to determine the effects of the varied duct throat separation on the performance of the proposed variable geometry radial flow ejector, this was measured in terms of entrainment ratio and critical back pressure. The results showed an increase of 34% could be achieved by increasing the duct separation from 2.2 mm to 3.0 mm, however, this resulted in a decrease in critical back pressure. Conversely, an improvement in critical back pressure of over 40% was achieved by reducing the duct separation from 3.0 mm to 2.2 mm.

It was concluded that the concept was a viable solution to the variable geometry ejector problem, and as such experimental studies on a physical prototype should be performed. Data from the experiments would then allow for validation of a CFD model suitable for further development and optimisation.

2.6.4 Experimental Evaluation of a New Radial Ejector Design

The overall design of the radial flow device encompassed a supersonic nozzle inside an ejector duct arrangement as shown in figure 2.5. Al-Doori's (2013) axial flow ejector was used in the experimental testing as a benchmark and to set the target parameters for the radial design.

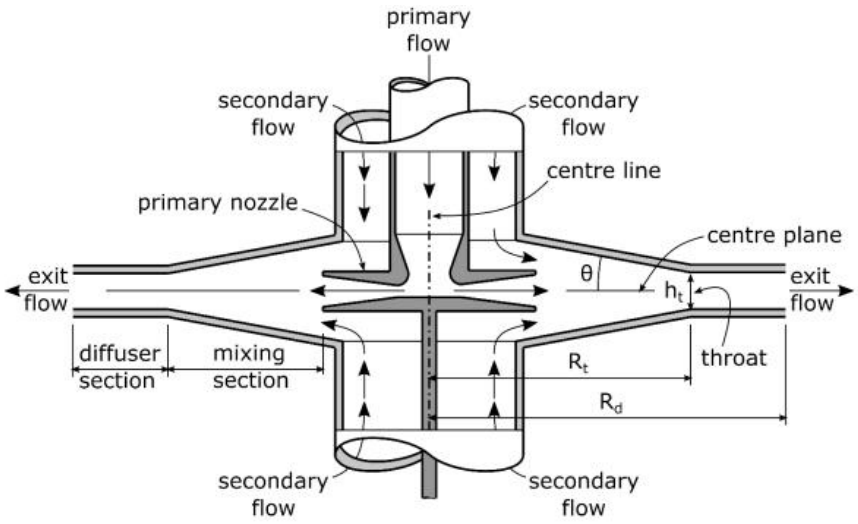

Figure 2.5: Diagram of the novel radial ejector design and its flow paths.

The radial flow supersonic nozzle has the same features as an axial variant with a constant cross-sectional area inlet, a convergent section, a throat, and a divergent section. The constant cross-sectional area inlet was set to 30 mm, this was the maximum allowable due to fabrication constraints. The nozzle throat separation was defined to be 0.4 mm at a radius of 3.5 mm, this gave a throat area of 8.8 mm^2. The throat area was approximately 9% larger that the axial nozzle to accommodate for an assumed lower discharge coefficient as a result of the sharp flow direction changes in the radial nozzle. The nozzle exit area was chosen to be 180 mm^2 giving an AR of 20.4 compared to the axial device with an AR of 18.1, this was to achieve a defined nozzle exit Mach number as set by the axial flow design. Considerations were made for the divergent angle and resolved to set it equal to the axial device at 5°, resulting in a radial length for the nozzle divergent section of 9.5 mm compared to 59.5 mm for the axial design. Subsequently, this feature allowed for a much smaller wetted area in the nozzle and therefore less frictional losses in the flow.

The design of the ejector duct began by specifying an AR of 59 and an ejector throat area of 520 mm^2, values that were deemed in close agreement with the benchmark axial ejector design. Traditional axial ejector design procedures could not be used directly but were used as a basis for the radial design. As mentioned earlier, all efforts were made to produce a radial flow device that matched the performance of the benchmark axial flow ejector, however, some considerations were essential due to fabrication limitations. Figure 2.6 shows a sectioned 3D drawing of the radial flow prototype design and a comparison of the geometric parameters for the axial and radial ejectors given in table 2.3.

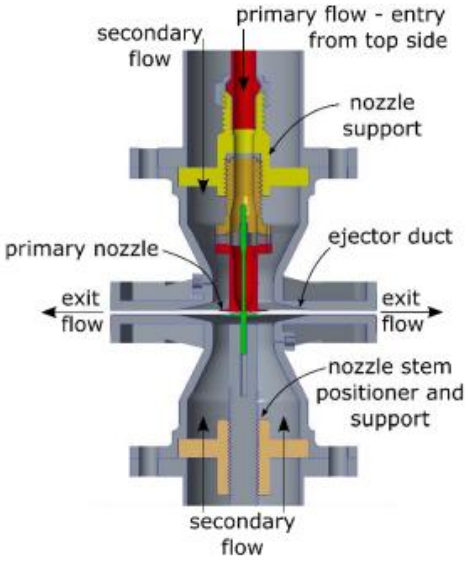

Figure 2.6: Rendered drawing of radial ejector prototype.

Table 2.3: Comparison of radial ejector prototype to equivalent axial ejector dimensions.

Axial Ejector		**Radial Ejector**	
Dimension	**Value**	**Dimension**	**Value**
Nozzle throat diameter (mm)	3.2	Nozzle throat radial distance (mm)	3.5
Nozzle exit length (mm)	59.5	Nozzle throat separation (mm)	0.4
Nozzle exit diameter (mm)	13.6	Nozzle exit radial distance (mm)	13
Nozzle throat to mixing section entrance distance (mm)	59.5	Nozzle exit separation (mm)	2.2
Mixing section entrance diameter (mm)	37	ejector contraction half-angle	9°
Nozzle throat to ejector throat entrance distance (mm)	214.5	Ejector throat radial distance (mm)	36
Ejector throat diameter (mm)	25.4	Ejector throat separation (mm)	2.3
Nozzle throat to ejector throat exit distance (mm)	289.5	Ejector exit radial distance (mm)	72
Nozzle throat to diffuser exit distance (mm)	499.5	Valve stem diameter (mm)	1.8
Diffuser exit diameter (mm)	50	-	-
Nozzle throat area (mm^2)	8.04	Nozzle throat area (mm^2)	8.8
Nozzle exit area (mm^2)	145	Nozzle exit area (mm^2)	180
Nozzle area ratio	18.1	Nozzle area ratio	20.4
Divergent part length (mm)	59.5	Divergent part length (mm)	9.50
Divergent half angle	5°	Divergent half angle	5°
Nozzle wetted area (mm^2)	1590	Nozzle wetted area (mm^2)	990
Ejector throat area (mm^2)	507	Ejector throat area (mm^2)	520
Ejector Diffuser exit area (mm^2)	1960	Ejector Diffuser exit area (mm^2)	1040
Ejector area ratio	63	Ejector area ratio	59
Ejector flow length (mm)	500	Ejector flow length (mm)	68.5
Ejector wetted area (mm^2)	92500	Ejector wetted area (mm^2)	31800

Figure 2.7 shows a schematic of the experimental setup used to test the radial flow prototype, and an illustration of the radial ejector connected to inlet piping and a receiving tank is shown in figure 2.8.

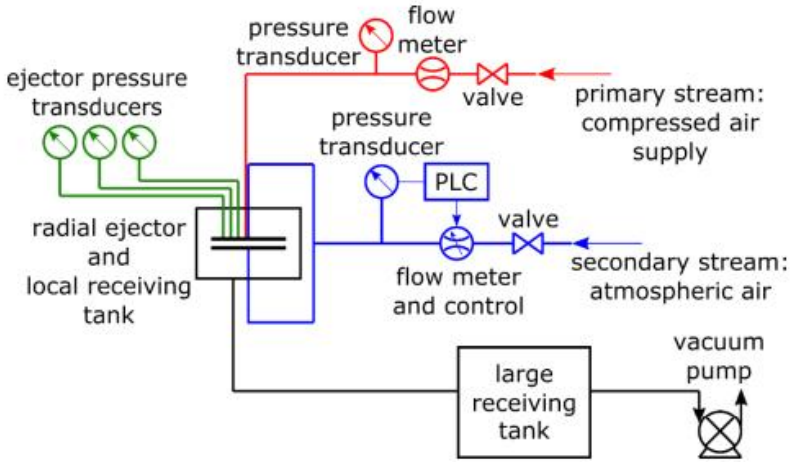

Figure 2.7: Schematic of Rahimi's experimental apparatus.

The primary flow rate and pressure were controlled with a ball valve and pressure regulator after the primary mass flow rate was calibrated as a function of pressure with the use of a mass flow meter. This mass flow meter was then attached to the secondary stream with a programmable logic controller (PLC) to control the secondary mass flow rate during the experiment. This was needed to ensure a constant secondary inlet pressure was maintained while while the local receiving tank pressure increased. Four pressure transducers were also placed throughout the setup for pressure data collection

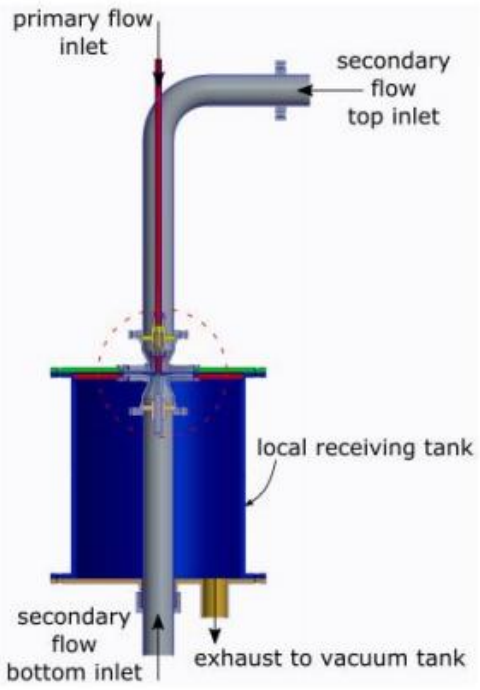

Figure 2.8: Illustration of original VGRE installed in experimental setup.

A quasi one-dimensional gas dynamic simulation was performed for initial comparison to the collected experimental data. The modelling was calibrated via direct comparison to actual ejectors with respect to the entrainment ratio and the critical pressure lift ratio. It was determined that the entrainment ratio values of the model were adequate for comparison, but the critical pressure required an adjustment which ultimately provided an uncertainty level of around ±20%.

A series of experiments were performed for operating conditions with primary pressures of 160, 200, and 250 kPa, and secondary pressures of 1.8, 2.5, and 3.2 kPa. When compared to the quasi one-dimensional gas dynamic model the experimental results showed good agreement for the entrainment ratio values. However, the critical pressure lift ratio did not perform as expected compared to the model. Rahimi speculated that it may be due to several factors, namely, an insufficiently large mixing section in the ejector, or an excessive rate of pressure rise in the diffuser section. Regardless, it was decided that the concept worked well enough to continue with further development and experimentation.

2.6.5 Experimental Investigation of Radial Ejector Performance

In order to determine the cause of the critical back pressure shortcomings discovered in the first experimental investigation of the prototype, a second set of experiments was devised to investigate the flow behaviour through the device by measuring and analysing the static wall pressure at the ejector throat for a variety of operating conditions. Pressure measurements were achieved by installing pressure transducers into the top plate of the ejector duct at varying radial distances. An assumption that pressure should be independent of the angular position due to the symmetry of the device was employed, allowing for more transducers to be placed than if they were in a single radial line. The arrangement of the transducers is shown in figure 2.9.

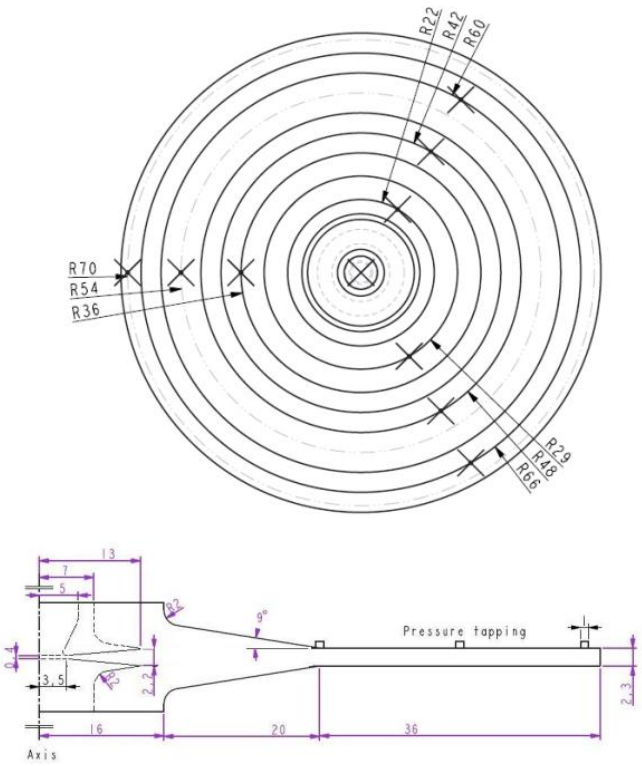

Figure 2.9: Dimensioned drawing of pressure tapping placement in the ducts.

The same experimental hardware and setup procedures were used to run the second set of experiments, as were the operating conditions that were tested. The results of the experiments allowed Rahimi to identify several flow behaviours through the radial ejector, these included:

- An increase in primary flow pressure would decrease the entrainment ratio and increase in the pressure lift ratio.
- An increase in secondary flow pressure would increase both the entrainment ratio the pressure lift ratio.
- When operating in critical mode, the static pressure at the physical throat is always higher than the isentropic choking value of the secondary stream.
- For all configurations, when operating in critical mode, the unmixed portion of the secondary stream at the throat was calculated to have a Mach number of approximately 0.7.
- In sub-critical mode, the rate of entrainment ratio decrease and the rate of throat pressure change with increasing exit pressure is not constant, contrary to the typical behaviour of axial ejectors.
- An audible noise was detected for some operating conditions suggesting an oscillatory flow was present.

2.6.6 CFD Simulation of Radial Flow Air Ejector Experiments

As a result of the discrepancies between the previously performed computational simulations and experimental data, analyses identified several potential reasons for the under-performance of the physical device compared to the simulations. Inaccurate nozzle and ejector throat separations in the manufacture of the device and other radial ejector geometry limitations were expressed, as were high adverse pressure gradients. These factors were investigated further, computationally, to ascertain any relevance they have to the performance issues.

The simulation parameters used previously and outlined in table 2.2 were once again used to perform the simulations with one difference, the turbulence model used this time was the standard k-ϵ model. Data presented by Rahimi et al.(2016), and Rahimi et al. (2017) were also used for comparison, providing results for SST k-ω simulations. ANSYS Fluent 16.1 was employed this time to perform the calculations and as such new geometry was drawn and meshed for the new simulations. A mesh independence study was also performed resulting in a mesh consisting of 51451 elements.

A comparison of the entrainment ratio and critical back pressure with respect to the expansion ratio for the two turbulence models and the experimental results determined that the SST k-ω model always overestimates the values. Whereas the standard k-ε model underestimates the entrainment ratio at lower expansion ratios and overestimates at higher expansion ratios, and for the critical back pressure it underestimates at lower expansion ratios but approaches parity as the expansion ratio increases.

An analysis of the Mach number found that the primary stream achieves supersonic conditions in the diverging section of the nozzle with a sequence of oblique wave structures forming through the mixing section of the ejector. A maximum Mach number of approximately 4.25 was determined which was mostly unaffected by change in the back pressures, this value was claimed comparable to results previously determined for axial flow ejectors (Ruangtrakoon et al. 2013), (Chandra & Ahmed 2014). Rahimi also stated that unlike typical axial flow ejectors that accelerate the secondary flow to sonic conditions, the current radial configuration is incapable of achieving such velocities in the secondary flow.

The study showed that the wall pressures for both turbulence models provided poor agreement with the experimental data. A high pressure zone near the physical throat was simulated by both models, a feature that was not present in the experiments. The standard k-ε model simulated

pressure peaks higher than the exit value for all operating conditions. The SST k-ω model was considered to have better agreement to the experimental data as it did not overestimate the pressure near the throat when operating in sub-critical mode.

The simulations identified flow separation in the mixing region of the radial ejector and subsequently a new model was developed with a smooth profile near the ejector throat to investigate the effects. These modifications provided a larger ejector throat area than the previous design but were useful for investigating the behaviour of the flow separation, which resulted in a changed position and a reduction of the asymmetry of the recirculation zone, this is depicted in figure 2.10.

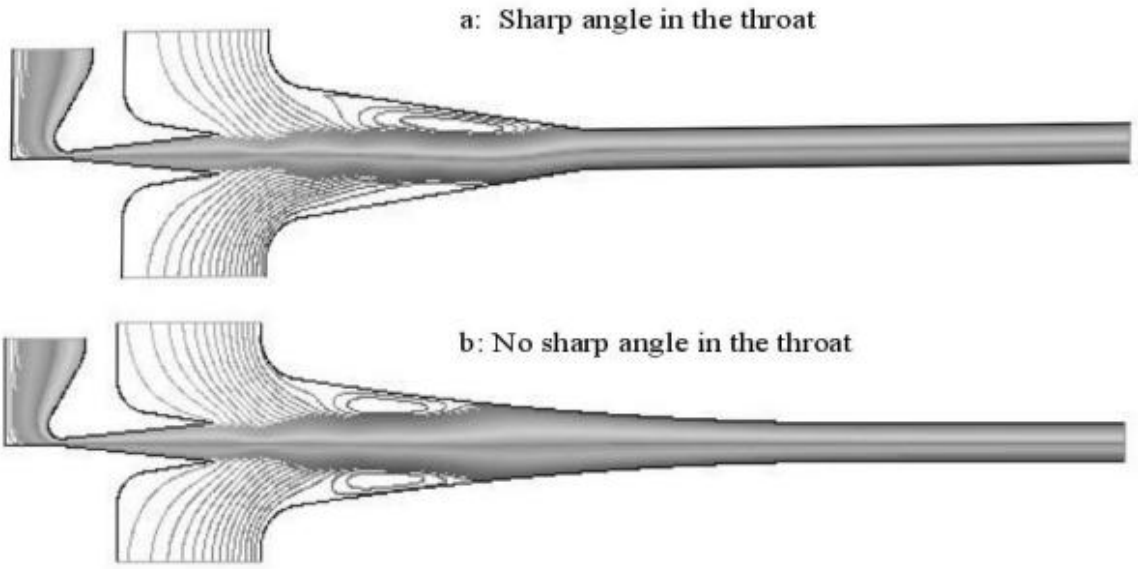

Figure 2.10: Comparison of duct profile changes at the ejector throat.

It was suggested that the flow separation may be caused be the rate of change of cross-sectional area in ejector duct being too small. As a result Rahimi suggested a new flow cross-sectional area profile, as shown in figure 2.11. This profile was also designed to mitigate adverse pressure gradients in the diffuser section and introduce a constant area zone in the throat region. Initial simulations of the suggested profile, however, determined it to be an unsuccessful design and Rahimi conceded that further work was needed to optimise the cross-sectional flow area.

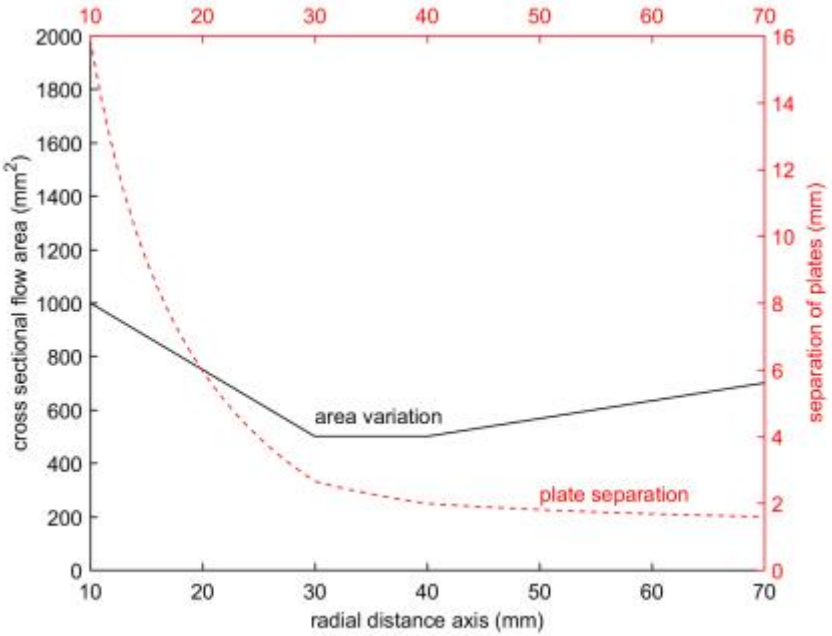

Figure 2.11: Suggested profile for cross-sectional area and plate separation for an improved VGRE.

2.6.7 Conclusions and Further Work

Upon completion of his investigations, Rahimi concluded that entrainment ratios comparable to axial ejectors can be achieved with a radial flow configuration but further optimisation was required to increase critical exit pressures. He identified the following areas of research that would be required for further development of the VGRE device:

- Improvement of flow profiles to reduce pressure losses.
- Investigation into lift ratio underperformance, causes and improvements.
- Development of applicable radial ejector design approaches.
- Investigation of nozzle adjustability and its effects on performance.
- Experimental investigation of all adjustability options for the ejector.
- Optimisation of CFD models and investigation of alternative turbulence models.
- Investigation into the oscillatory flow behaviour identified in the radial ejector.

2.7 Improved VGRE

2.7.1 Introduction

Following the work presented by Rahimi (2017) in his thesis, recommendations were taken on board by Raed Al-Rbaihat (2020) in his own thesis to investigate and develop the variable geometry radial ejector device that is also the focus of this dissertation. The following sections are a review of the work presented by Al-Rbaihat in his thesis, where an investigation into alternative CFD turbulence models was performed, improvement of the VGRE design was investigated, new experimental investigations were performed, and a validation analysis of the CFD results with respect to the new experimental data was provided.

2.7.2 CFD modelling of the original VGRE

As per the recommendations for further work identified by Rahimi (2017), a series of simulations were performed using the original radial ejector geometry to ascertain a turbulence model that provided the best agreement to the experimental data collected for the original device (Rahimi 2017). This study analysed the results of five Reynolds Averaged Navier-Stokes (RANS) turbulence models and five Detached Eddy Simulation (DES) turbulence models, and a comparison was performed for the best of each model type. It was also determined that transient simulations would be utilised as they offer better converged solutions compared to steady state simulations (Park et al. 2008; Jafarian et al. 2016; Arun Kumar and Rajesh 2019). In addition to investigating the best turbulence model, Al-Rbaihat also took the opportunity to investigate how the nozzle and duct separations would affect the simulations at the same time. This was done by producing model geometries consisting of 0.4, 0.5, and 0.6 mm nozzle separations, and 2.3, 2.6, and 3.0 mm duct separations, resulting in a total of nine geometries.

All simulation parameters and boundary conditions were the same as those for the simulations performed by Rahimi (2017), outlined in table 2.2, with the exception of the aforementioned transient configuration which employed a time step size of $5e^{-6}$ seconds, for a total of 10,000 time steps, with a maximum of 150 iterations per time step. A Courant number of 1 was also employed for the transient simulations. A mesh independence study was performed and mesh counts of approximately 70,000 to 85,000 elements for the various geometries was determined to be computationally efficient while remaining adequately accurate.

In performing the CFD investigation of the original VGRE, values for the entrainment ratio and critical outlet pressure for the five RANS and five DES models were compared to the experimental data collected by Rahimi (2017), shown in table 2.4. The parameters for this study were primary pressure of 200 kPa, secondary pressure of 1.8 kPa, nozzle separation of 0.5 mm, and duct separation of 2.3 mm. For both the RANS and DES type models it was determined that the best agreement was shown by the SST k-ω turbulence model, with the DES SST k-ω model being the better of the two simulating the entrainment ratio and critical outlet pressure with 0.3% and 56.75% error respectively. These turbulence models were chosen for comparison sake moving forward with development of the VGRE.

Table 2.4: Comparison of CFD results to experimental data of original VGRE.

Model	ω - EXP	ω - CFD	Error (%)	P_o^* (kPa) - EXP	P_o^* (kPa) - CFD	Error (%)
RANS Models						
SST k-ω	0.29	0.376	29.7	2.84	5.00	76.1
Realizable k-ϵ	0.29	0.420	44.8	2.84	5.32	87.3
Spalart-Allmaras	0.29	0.392	35.2	2.84	5.22	83.8
Transition SST	0.29	0.428	47.6	2.84	5.51	94.0
BSL k-ω	0.29	0.383	32.1	2.84	5.10	79.6
DES models						
DES SST k-ω	0.29	0.289	0.3	2.84	4.45	56.7
DES Realizable k-ϵ	0.29	0.424	46.2	2.84	5.05	77.8
DES Spalart-Allmaras	0.29	0.281	3.1	2.84	3.80	33.8
DES Transition SST	0.29	0.286	1.4	2.84	3.90	37.3
DES BSL k-ω	0.29	0.289	0.3	2.84	4.70	65.6

All simulations were performed using ANSYS Fluent and assessed against the experimental results. The analysis showed that the DES SST k-ω model offered an error of approximately 5% for the mass flow rate, and and average error 5% for entrainment ratio for all separation configurations simulated. Whilst these were considered good agreement the critical compression ratio was still overestimated as it was for the RANS model.

The range of values simulated for the varying separation configurations gave entrainment ratios of between 0.16 and 0.61, critical outlet pressures of between 2.64 and 5.53 kPa, and critical compression ratios of between 1.5 and 3.1, for the operating conditions that were investigated. This showed good insight into the relationship between the performance of the ejector and the operating and geometric parameters. An outline of these relationships is given in table 2.5.

Table 2.5: Relationships between parameters and performance metrics.

Parameter	**Performance Outcomes**
$P_p \uparrow$	$\omega \downarrow , P_o^* \uparrow , r_c^* \uparrow$
$P_s \uparrow$	$\omega \uparrow , P_o^* \uparrow , r_c^* \uparrow$
$r_e \uparrow$	$P_p \uparrow , P_s \downarrow$
$r_e \uparrow$	$\omega \downarrow , P_o^* \uparrow , r_c^* \uparrow$
$d \uparrow$	$\omega \downarrow , P_o^* \uparrow , r_c^* \uparrow$
$D \uparrow$	$\omega \uparrow , P_o^* \downarrow , r_c^* \downarrow$

Al-Rbaihat speculated that the asymmetric flow observed in the simulations may be a result of oscillation which could affect the entrainment ratio results for unchoked operating conditions and also postulates that the behaviour is due to an insufficient diverging part length in the primary nozzle.

Al-Rbaihat resolved that the best turbulence model for continued VGRE development was the DES SST k-ω model, although it performed poorly for off-design conditions it simulated well for on-design conditions. It was also noted that previous work has stated DES models are best employed in 3D simulations (Kubacki & Dick 2010; Zhou et al. 2018), and suggested that off-design operation should be investigated further using the 3D model. However, it was concluded that the current work would continue with simulations using 2D axisymmetric simulations.

2.7.3 Performance improvement to the original VGRE

A numerical investigation into the geometric features of the VGRE, depicted in figure 2.12, was performed to develop an improved version of the device. This study focused on the effect of four factors: the flow path angle; the diffuser geometry; the nozzle geometry; and the mixing chamber geometry.

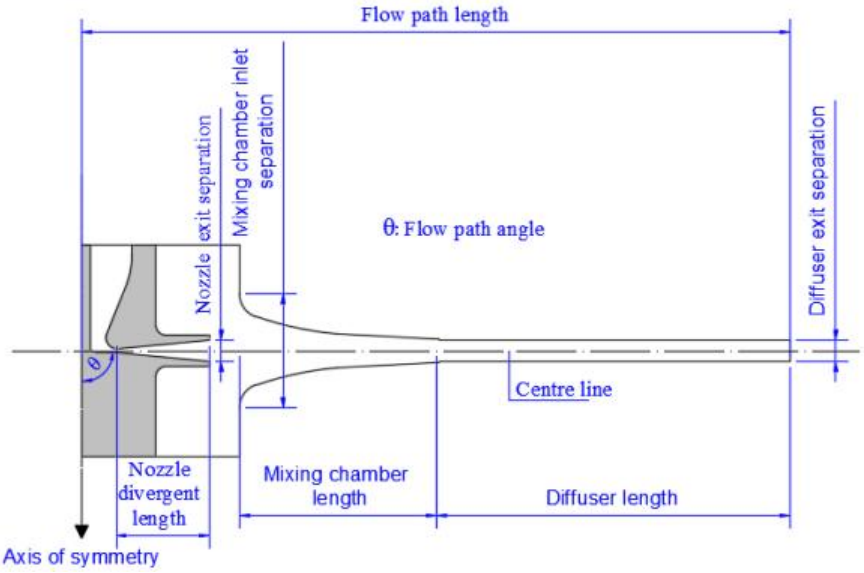

Figure 2.12: Diagram of geometric features of original VGRE.

The original VGRE utilised a flow path that exited at 90° to the direction of the primary flow. As an alternative to this, models were developed to simulate flows that exited at 45° and 60° relative to the primary flow to determine their affect on performance. These were created with the same ejector AR of 47 for easy comparison. However, upon analysis of the entrainment ratio, critical compression ratio, and isentropic efficiency values determined by the simulations. It was concluded that whilst there were some improvements in critical compression ratio there were also decreases in entrainment ratio and overall the average efficiency ultimately decreased by approximately 10%, resolving to keep the flow path at the original 90° configuration.

An investigation into the effect that the diffuser AR has on the entrainment ratio, critical compression ratio, and the isentropic efficiency of the ejector was performed by altering the length of the diffuser section. Lengths of 18, 24, 36, 54, and 72 mm were modelled to simulate diffuser ARs of 1.5, 1.7, 2.0, 2.5, and 3.0 respectively. Previous studies in the literature had defined diffuser ARs of less than 5.0 as being an appropriate value (Rusly et al. 2005; Zhu et al. 2009; Al-Doori 2013; Wu et al. 2014; Wu et al. 2018). The results of this investigation determined that for the diffuser ARs studied there was a maximum of 1% improvement in entrainment ratio; a maximum of 1% improvement in critical compression ratio; and approximately 2% improvement in ejector efficiency, compared to the design of the original VGRE. Since the improvements were found to be only minor the diffuser AR was maintained at the value of the original VGRE of 2.0 corresponding to a diffuser length of 36 mm.

The nozzle geometry was next to be investigated, focusing primarily on the nozzle AR. In order to maintain the overall radial ejector geometry it was decided that the nozzle throat and exit would remain constant and the AR would be varied by altering the nozzle divergent section length instead. Divergent lengths of 7.5, 8.5, 9.5, 11.5, and 12.5 mm were chosen to give corresponding nozzle ARs of 13.8, 15.1, 16.4, 18.8, and 20.1 respectively. These geometries were simulated using different primary pressures and their entrainment ratios, critical compression ratios, and isentropic efficiencies were analysed. The maximum improvements for the three criteria were 4%, 3%, and 6% respectively. The results were decided to be too insignificant to implement changes into the improved VGRE design and as such the original nozzle divergent length of 9.5 mm was maintained.

The final feature investigated was the mixing chamber geometry, a factor that has been previously identified as very important in ejector performance (Wongwises & Disawas 2005; Chaiwongsa & Wongwises 2008; Zhu et al. 2009; Wu et al. 2014; Palacz et al. 2016; Jeon et al. 2017; Ramesh and Sekhar 2018). The mixing chamber analysis was performed by altering the length of the mixing chamber while keeping the convergence angle and exit separation of the section constant. Doing this also resulted in the inlet of the mixing section increasing with the increased length. Simulations were performed for varying primary pressures at a constant secondary and outlet pressure. An analysis of the entrainment ratio showed an average improvement of approximately 54% when the ejector AR was increased from 47 to 67, corresponding to a mixing chamber length of 35 mm and inlet separation of 20 mm. The entrainment ratio decreased for ARs greater than 67 for all primary pressures. Conversely, however, an analysis of the critical compression ratio determined an average decrease of approximately 11% for the primary pressures simulated. Though performance was best with only a 3% reduction at the highest primary pressure of 250 kPa. Additional investigation into the critical compression ratio suggested that improvements could be achieved for higher primary pressures by altering the nozzle and duct separations. The isentropic efficiency was found to increase an average of 28% over the different primary pressures for an ejector AR of 67. However for the lowest primary pressure of 160 kPa the performance was best with an AR of 56 instead. It was ultimately determined that adopting an ejector AR of 67 into the design of the improved VGRE would be beneficial.

2.7.4 Potential benefits of the improved VGRE

One of the primary applications for the improved VGRE is for use in refrigeration systems that utilise solar energy. These systems would greatly benefit from a variable geometry ejector due to their

transient operating conditions affecting the efficiency of the cycle. Another consideration that should be made, however, is the type of working fluid used and how well the VGRE can operate with it. The principle working fluid for all previous studies performed for the original and improved VGRE has been air. As an alternative, steam has been considered as a potential working fluid also and as such it was decided to investigate its behaviour with CFD simulations.

An ideal gas modelling approach was used to provide a comparison between air and steam as a working fluid. These simulations used the DES SST k-ω turbulence model and were run for a number of expansion ratios by varying the primary pressure and keeping the secondary pressure constant. The results of the comparison showed a variance of about 3% for the entrainment ratio and 4% for critical outlet pressure over the different expansion ratios. Determining the model suitable for both air and steam working fluids.

To assess the suitability of the improved VGRE further, modelling of a steam ejector cooling system, depicted in figure 2.13, was conducted to evaluate the overall performance of the system under a variety of primary stream operating conditions with different nozzle throat separations. Although it has been reported that this simplified configuration is physically impracticable (Hemidi et al. 2009; Ruangtrakoon et al. 2013) for steam as a working fluid, it was considered sufficient for the purpose of comparing the improved VGRE and a fixed ejector at this stage.

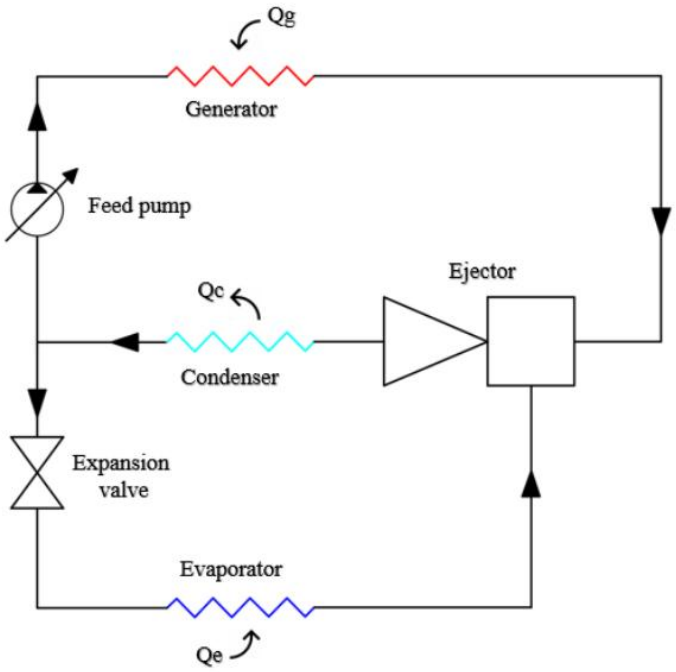

Figure 2.13: Schematic diagram of steam ejector cooling system.

The simulation was prepared in Matlab to inspect the performance of the system using local insolation data for one clear day and one cloudy day. A net cooling improvement of 11% was identified for the clear day simulations when using the improved VGRE compared to the fixed geometry ejector, and likewise a 6% improvement was identified for the cloudy day data. Whilst these were considered modest improvements, Al-Rbaihat noted that they were based on nozzle throat separations of 0.4, 0.5, and 0.6 mm only and that a larger value range with smaller increments would simulate greater improvements. Additionally, it should be reiterated that this was a simplified model and as such further refinement of the analysis is possible if better reliability of the results is required.

2.7.5 Apparatus design

The design of the experimental apparatus used for testing the improved VGRE was described to great detail with system schematics, assembly drawings, and detailed part drawings with dimensions. The overall design was based on the apparatus used by Rahimi (2017), but was adapted to enable adjustment of the nozzle and duct throat separations for more extensive experimentation. Figure 2.14 shows a 3D rendering of the VGRE attached to the primary and secondary inlet flow pipes as well as the outlet receiving tank.

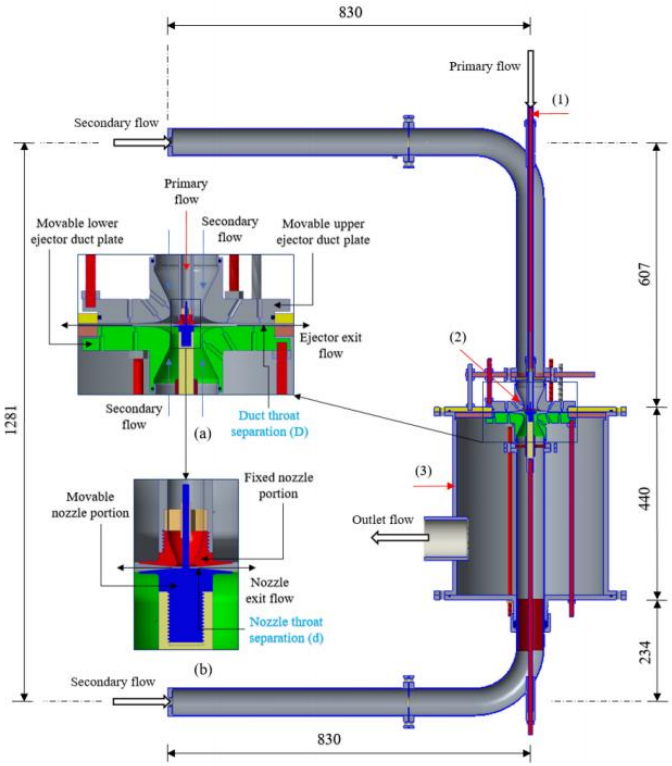

Figure 2.14: Rendered drawing of improved VGRE installed in experimental apparatus.

The dimensioned drawings shown in figures 2.15(a) and 2.15(b) depict the geometry of the supersonic variable nozzle and the duct plates that comprise the VGRE that is to be simulated for this dissertation. The lower half of the nozzle is shown with a centering pin which extends through the upper half of the nozzle inside the primary flow pipe and rests in a centraliser to keep the radial flow symmetrical. The ejector flow path is created using two symmetrical duct plates which were both capable of adjustment, this ensured the flow path was centered on the ejector exit when separation adjustments were made.

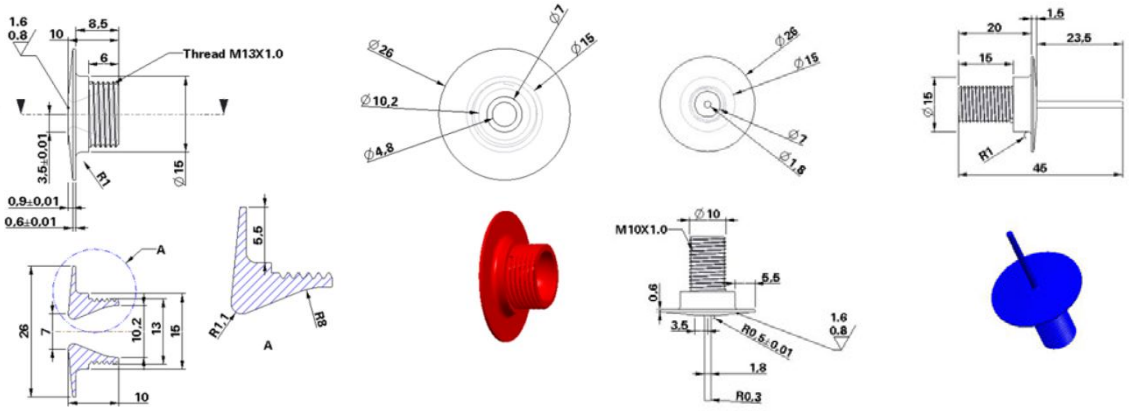

Figure 2.15(a): Engineering drawings of improved VGRE supersonic nozzle, top and bottom pieces.

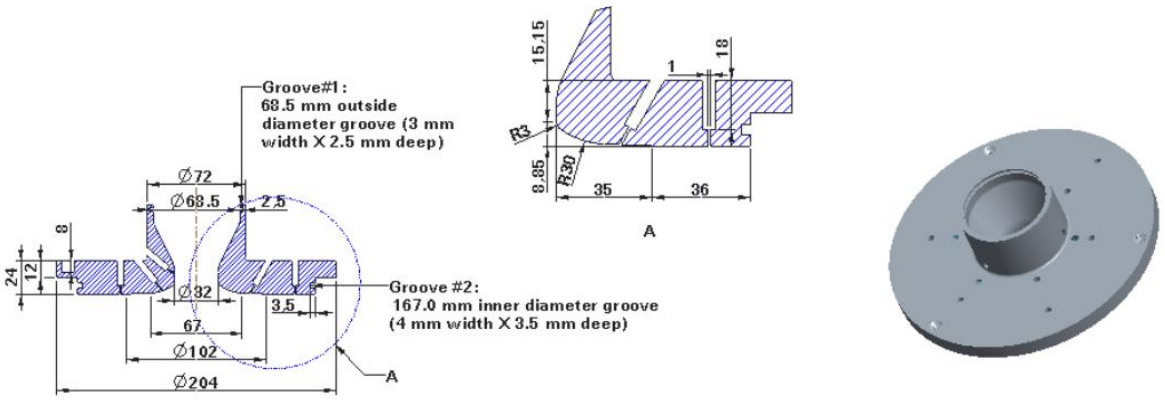

Figure 2.15(b): Engineering drawings of symmetrical duct plate.

The duct plates were also installed with 12 pressure transducers each to collect the data required to investigate the flow behaviour. In addition to the pressure transducers, thermocouples were installed in the system to measure the temperature of the primary, secondary, and outlet streams; flow meter controllers were used to measure the primary and secondary mass flow rates; and a

data acquisition system was used to collect the measured data. A photograph of the entire experimental system is given in figure 2.16, labeling its main features.

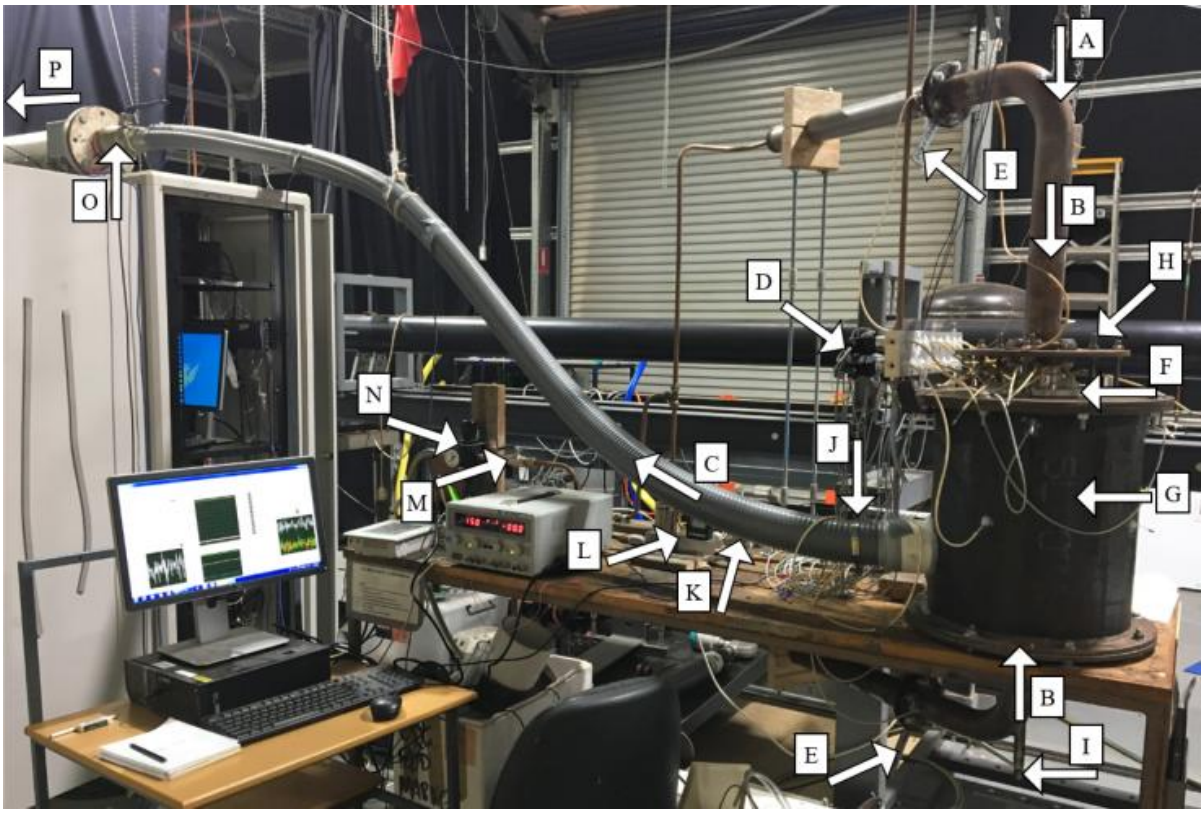

Figure 2.16: Photograph of experimental apparatus.

(A) primary supply line,
(B) secondary flow line,
(C) outlet line connected to vacuum system,
(D) pressure transducers,
(E) orifice plate,
(F) upper ejector duct plate,
(G) receiving tank,
(H) control rods to adjust the upper ejector duct plate,
(I) control rod to adjust the lower nozzle portion,
(J) data acquisition,
(K) PLC,
(L) flow meter controller,
(M) control valve of the primary pressure,
(N) pressure regulator,
(O) ball valve to access the vacuum system,
(P) vacuum system.

2.7.6 Experimental investigation of the improved VGRE performance

Before any experimental testing of the VGRE was performed a series of preliminary tests were conducted to ensure all equipment was properly calibrated and operating reliably and consistently.

This also allowed for an experimental procedure to be defined before the main experiments were performed. An uncertainty analysis was also performed to determine the accuracy for the entire experimental system.

Constant pressure values were essential for the experiments, so the stability of the system was assessed as part of the preliminary tests for both the primary and secondary pressures. These tests determined a reduction in primary pressure of approximately 0.8% for a nominal pressure of 200 kPa, over the typical test time duration of about 100 seconds. A reduction in the primary flow temperature of approximately 0.6% was also observed. A nominal secondary pressure of 1.8 kPa was also tested with an observed pressure increase of about 2.2%, this was due to a mass build up in the receiver tank, but was being mitigated by a PLC to maintain a constant pressure. The secondary flow temperature stayed approximately constant for the duration of the test.

System repeatability was tested by conducting all tests twice for varying primary pressures. The results determined a maximum variability of approximately ±4.6% for the entrainment ratio and ±5.0% for the critical outlet pressure between the repeated tests. The static pressure along the wall showed good consistency with the maximum variability being less than ±2% between the repeated tests at all tested conditions.

The uncertainty analysis was performed based on the manufacturers' data for accuracy, for each of the measurement devices in the system. These devices included pressure transducers (PT), a flow meter device (FMD), thermocouples (TC), and a barometer (Ba). The root sum of squares method, as described by Van Nguyen et al. (2020), was employed to determine the total uncertainty for each measured parameter, the details of which are given in table 2.6.

Table 2.6: Uncertainty calculations for each measured experimental parameter.

Measured Parameter	**Measuring Device**	**Uncertainty (%)**	**Total Uncertainty (%)**
P_p	PT, Ba	0.5, 0.01	0.5
P_s	PT, Ba	0.5, 0.01	0.5
P_o	PT, Ba	0.5, 0.01	0.5
$\dot{m}_p$	PT, FMD, Ba	0.5, 0.8, 0.01	0.9
$\dot{m}_s$	FMD	0.8	0.8
ω	PT, FMD, FMD, Ba	0.5, 0.8, 0.8, 0.01	1.2
T	TC	0.7	0.7

With full consideration for these uncertainties along with the system stability and repeatability, systematic error, and noise associated with the electrical and data acquisition systems, it was suggested that the entrainment ratio and critical outlet pressure values retrieved during experimentation would be accurate to within ±3%.

The main experiments involved a series of test that incorporated primary pressures of 160, 200, 250, 270, and 300 kPa, and secondary pressures of 1.2, 1.5 , and 1.8 kPa, resulting in critical outlet pressures ranging from 2.4 kPa to 8.0 kPa. Nozzle throat separations of 0.4, 0.5 and 0.6 mm, and duct throat separations of 2.3, 2.6 and 3.0 mm were used, to give ARs ranging from 59 to 109. The consequential entrainment ratios, critical compression ratios, and expansion ratios are expressed in table 2.7 as ranges of calculated values.

Table 2.7: Various performance ratio ranges calculated from experimental data.

Performance Parameter	**Value Range**
Entrainment ratio	0.29 - 1.26
Critical compression ratio	1.35 - 4.43
Expansion ratio	89 - 167

The maximum isentropic ejector efficiency achieved for all operating conditions tested was 36%. This was achieved with primary and secondary pressures of 160 and 1.8 kPa respectively, and throat separations of 0.5 mm for the nozzle and 3.0 mm for the duct. It was postulated that this efficiency could be increased further with an increased range of adjustment. With respect to fixed geometry ejectors, it was determined that the improved VGRE had an overall average improvement of 146% for entrainment ratio and an overall improvement of 100% for critical compression ratio, exhibiting the benefits that the improved VGRE offers.

A comparison was performed for the experimental results and a one-dimensional gas dynamic model that was previously simulated. This analysis identified average discrepancies of approximately 15% and 37% for the entrainment ratio and critical compression ratio respectively, for all cases tested. The improved VGRE was also compared to several previous studies of air ejectors with respect to performance. This analysis found an average improvement of 107% and 76% for the entrainment ratio and critical compression ratio. It also identified the average isentropic efficiency improved by about 18% relative to equivalent axial ejectors.

Al-Rbaihat concluded by stating that the results of the experiments with the small dimensional ranges tested, suggested that the improved VGRE should offer increased functionality over a larger range of nozzle and duct throat separations. It was also determined that the results were suitable for validating CFD simulations.

2.7.7 CFD model validation using the experimental data

Before the experiments were conducted on the improved VGRE, a series of CFD simulations were performed for the intended design and compared to experimental data collected by Rahimi (2017) for the original VGRE. This analysis determined the DES SST k-ω turbulence model showed the best agreement with the experimental results. However, upon comparing the results of the improved VGRE's experimental data to the DES SST k-ω turbulence model it was discovered that the level of agreement was not as accurate as first believed. It was speculated that dimensional accuracy was not fully achieved in the apparatus used for testing the original VGRE and as such the experimental data was not representative of the CFD simulations performed. As a result, additional CFD simulations were performed using the DES Realizable k-ϵ turbulence model for the improved VGRE and was compared along side the DES SST k-ω model to the experimental data for the improved VGRE. The Realizable k-ϵ model was chosen as it had been widely used in previous ejector simulations (Bartosiewicz et al., 2005; Ruangtrakoon et al., 2013; Zhu and Jiang, 2014b; Han et al., 2019).

The boundary conditions used in the simulations were set to the nominal values for the pressures as defined by the experimental investigation. The primary, secondary, and outlet temperatures were all set to the ambient temperature value, with the variance being considered too insignificant to affect the results. Table 2.8 shows the boundary condition values used for the various simulations. The parameters used for all simulations were maintained from the previously performed simulations as outlined in table 2.2, with the addition of the Realizable k-ϵ turbulence model.

Table 2.8: Boundary condition values used for various CFD simulations.

Boundary	**Pressure (kPa)**	**Temperature (K)**
Primary Inlet	160, 200, 250, 270, 300	300
Secondary Inlet	1.2, 1.5, 1.8	300
Outlet	2 - 8	300

The outcome of the comparison revealed that neither of the simulated turbulence models provided an accurate representation for all performance parameters over the range of geometries and operating conditions tested. One parameter that did perform well was the simulated primary mass flow rate that was predicted to within less than 1% accuracy of the experimental results. The comparison of the wall static pressures concluded that whilst the DES SST k-ω model predicted better agreement with the experimental results than the DES Realizable k-ϵ model, neither of the models provided good agreement. The Realizable k-ϵ model offered great prediction for the entrainment ratio with an average discrepancy of 5% compared to 24% for the SST k-ω, and both compared equally with respect to the critical compression ratio of an approximate 15% average discrepancy each. Although, a respective result of 3% and 1% for Realizable k-ϵ and SST k-ω models was simulated for the improved VGRE settings at: 0.4 mm nozzle separation; 2.3 mm duct separation; 250 kPa primary pressure; 1.8 kPa secondary pressure; and 3.0 kPa outlet pressure. Overall it was determined that the Realizable k-ϵ was the better of the two turbulence models, but it was also restated that 3D DES simulations provide a more reliable result compared to 2D because they allow the largest unsteady vortices to be resolved fully as reported by some studies (Kubacki & Dick 2010; Zhou et al. 2018).

2.7.8 Conclusions and further work

A review of the outcomes from Al-Rbaihat's work acknowledged that, due to previously collected erroneous data as a result of the dimensional inaccuracy of the experimental apparatus used, the subsequent efforts to further develop the variable geometry radial ejector had been somewhat impeded. Despite this hindrance, the experiments revealed that the improvements made to the design of the original VGRE resulted in a significant performance increase, particularly in entrainment ratio which was better than other reported radial and axial ejectors. It was conceded that more work was required to provide a suitable CFD simulation that adequately represents the flow behaviour through the VGRE. The following recommendations were made for future work:

- Further performance optimisation for nozzle and duct profiles.
- Experimentation and simulation using environmentally friendly refrigerants for usability in solar powered cooling systems.
- Investigation into auto-tuning of the radial ejector via electrical motors rather than manual adjustment.
- Study of new flow visualisation methods to obtain a better understanding of the radial ejector flow behaviour.

- CFD analysis investigating the oscillating flow behaviour present in some simulations.
- Optimisation of CFD models using 3D DES simulations to increase reliability of simulations.

This final recommendation has fostered the basis for the present work being undertaken with much of the information presented in Al-Rbaihat's (2020) thesis is fundamental to the work presented in this dissertation. The simulation parameters and boundary conditions expressed are to be used for advanced simulations and the experimental work performed will be used to validate these new simulations. It is the intention that by continuing the works of Rahimi (2017) and Al-Rbaihat (2020) that further development of the improved VGRE can be achieved.

Chapter 3

2D Simulations

3.1 Chapter Overview

The work presented in this chapter details the efforts made to achieve the project goals. Replications of geometries and meshes from simulations performed by Al-Rbaihat (2020) were produced and compared to the originals to determine their suitability for 2D simulations. The meshed geometries were then utilised to replicate the 2D simulations. The initial simulations were found to be quite time extensive and provided poor solutions. Multiple simulation variations were conducted to test various geometric features and operating conditions as a means to overcome the poor simulations but were also unsuccessful. Ultimately, the replication process was abandoned due to time constraints and focus was shifted towards the 3D DES simulations for the improved VGRE.

3.2 Introduction

The goal of the present work was to investigate the suitability of a 3D computational fluid dynamics model for simulating the flow characteristics of the improved VGRE as recommended by Al-Rbaihat (2020). This chapter discusses the the work performed in attaining the second objective from section 1.2 of this dissertation, to replicate the 2D CFD simulations performed by Al-Rbaihat (2020) and verify the results against the original simulations to provide understanding of the numerical processes that are required for analysing the improved VGRE.

All simulation work was performed using two machines: a personal laptop installed with ANSYS Fluent 2022R2 - Academic Version (licensed to the university and accessed via VPN) and 2024R2 - Student Version; and a High Performance Computer (HPC) accessed remotely and located at the University of Southern Queensland, Toowoomba campus, installed with ANSYS Fluent 2023R1 - Academic Version. The use of the HPC was employed to provided the computing power required for

time efficient solutions. Due to backwards compatibility problems with the ANSYS software, two versions were required on the personal laptop: 2022R2 was used to setup the simulations before transferring to the HPC to run the simulations; and 2024R2 was used to view the results after the simulations had been completed on the HPC. A description of all software and processes required to connect and operate the HPC remotely from the personal laptop was obtained from Cooper (2022).

Issues experienced during this phase of the project resulted in a sample simulation being obtained from Dr Raed Al-Rbaihat. This model featured a geometric configuration of 0.5 mm nozzle throat separation and 2.6 mm duct throat separation, and was used for comparisons of the geometry, mesh, and some simulations. The sample simulation that was acquired is referred to as the Al-Rb model throughout this work.

3.3 Geometry

Engineering drawings for the improved VGRE nozzle and duct, shown in figures 2.15(a) and 2.15(b) above, were obtained from Al-Rbaihat's (2020) thesis. However, there was some ambiguity in the dimensions of the duct profile, in particular the mixing section. Further research revealed drawings for the full improved VGRE assembly that were not provided in the thesis, shown in figure 3.1. Whilst this drawing provides a dimensional relationship between all parts of the device, it still presents with some ambiguity. The dimensions in question are the R3 and R30 radii that make up the top and bottom walls of the mixing section. All efforts were made to create a smooth transition through this region of the wall, but a level of uncertainty still remained for the accuracy of this feature. Additionally there was no defined angle between the converging separation of the mixing section and the constant separation of the diffuser section, at the duct throat, marked 'D' in figure 3.1. Visual inspection of the drawings for this feature was performed and an external angle of 178° was defined for use in the replicated geometries.

A total of nine geometries were created using DesignModeler to provide all combinations of nozzle and duct throat separations. The values to be tested were 0.4, 0.5, and 0.6 mm separations for the nozzle and 2.3, 2.6, and 3.0 mm separation for the duct. A nozzle half angle of 5° and nozzle diffuser length of 9.5 mm was used as per the findings of Al-Rbaihat's (2020) VGRE geometry optimisation analysis. An overview of the respective ARs for each geometry is given in table 3.1.

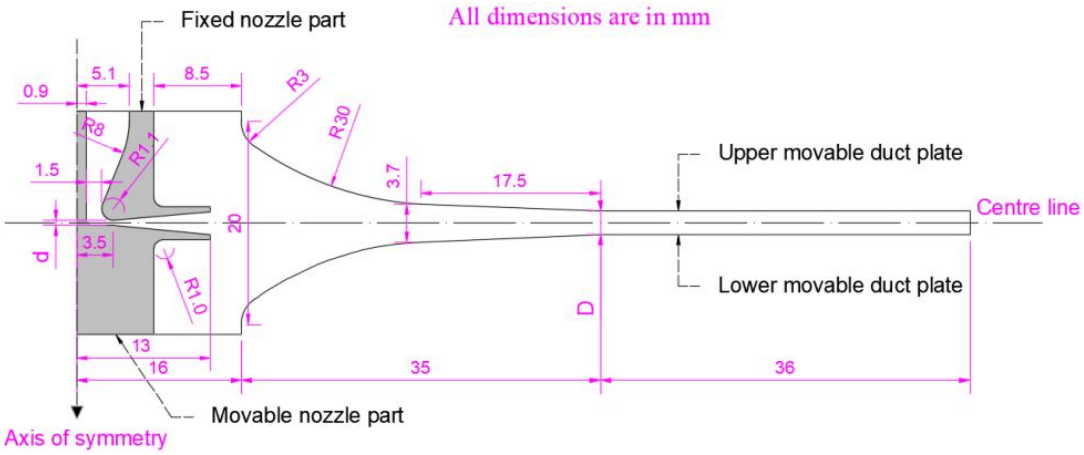

Figure 3.1: Dimensioned drawing of improved VGRE assembly (Al-Rbaihat et al. 2023).

Table 3.1: Geometry configurations and associated ARs.

Nozzle throat separation (d) mm	0.4	0.5	0.6	0.4	0.5	0.6	0.4	0.5	0.6
Duct throat separation (D) mm	2.3	2.3	2.3	2.6	2.6	2.6	3.0	3.0	3.0
Ejector area ratio (AR)	84	67	56	95	76	63	109	87	73
Nozzle area ratio (AR_n)	19.4	16.4	14.2	19.4	16.4	14.2	19.4	16.4	14.2

In order to provide a comparable mesh for the replication, the geometry was also sectioned using the face split tool to allow for a mesh refinement region in the primary nozzle and mixing section of the ejector, this will be discussed further in the next section. Named selections were created for the primary inlet, secondary inlets, outlet, and walls, to allow for the setting of the boundary conditions in the simulations.

3.4 Meshing

As part of the previous work, Al-Rbaihat (2020) performed a mesh independence analysis and determined that meshes of between approximately 70,000 and 85,000 elements were sufficient to provide reliable results for all the geometries in a computationally efficient manner. This set the target element count for the replicated 2D meshes. This target was achieved by setting the main element size to 3e-4 m with a default defeature size of 1.5e-6 m; applying three layers of inflation set with a smooth transition, transition ratio of 0.272, and growth rate of 1.2; and setting the element size for the refinement region to 6e-5 m. Figures 3.2(a) and 3.2(b) show the typical mesh that was generated for the model geometries.

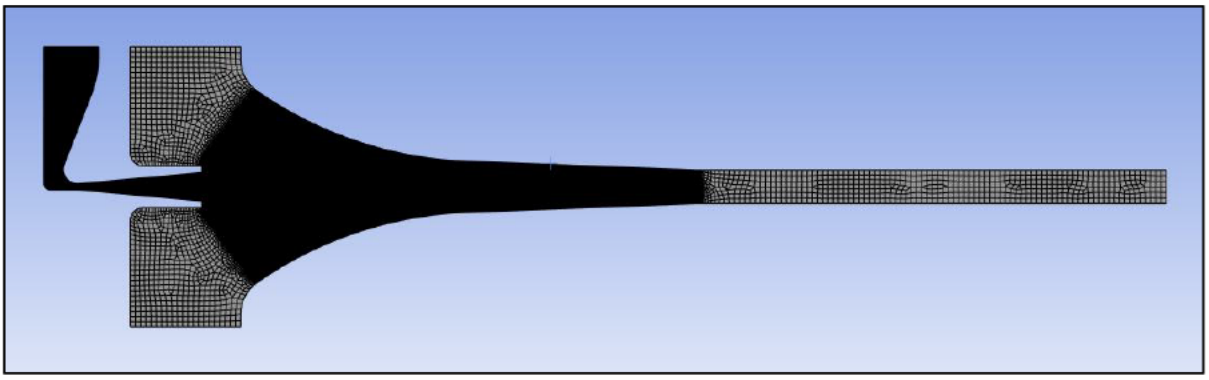

Figure 3.2(a): Meshing of the replicated geometry.

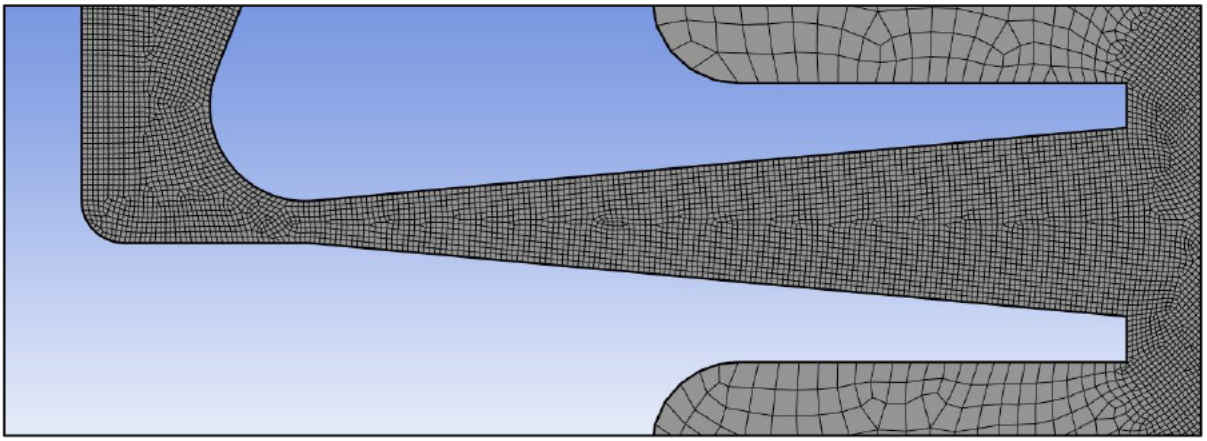

Figure 3.2(b): Zoomed view of refined mesh in the nozzle section.

Table 3.2 shows the element count for all geometry model meshes, these values all agree with the range stated by Al-Rbaihat (2020), and were therefore considered to be of adequate accuracy for the purpose of the replication simulations.

Table 3.2: Element count for each geometry configuration.

Nozzle throat separation (mm)	0.4	0.4	0.4	0.5	0.5	0.5	0.6	0.6	0.6
Duct throat separation (mm)	2.3	2.6	3.0	2.3	2.6	3.0	2.3	2.6	3.0
Number of elements	76097	79686	83702	78380	80145	83488	76623	80204	84575

3.5 CFD Parameters

The CFD simulations were setup to match the parameters and operating conditions expressed in the work performed by Al-Rbaihat (2020), utilising a density-based, transient solution for a 2D axisymmetric geometry. For the calculations the DES SST k-ω turbulence model was used with the energy equation turned on. The working fluid for the improved VGRE was air, which was modelled as an ideal gas, represented by the fluid density setting.

The boundary conditions used in the Al-Rbaihat (2020) simulations consisted of primary inlet pressures of 160, 200, 250, 270, 300 kPa; secondary inlet pressures of 1.2, 1.5, 1.8 kPa; and outlet pressures ranging between 2 and 8 kPa. However, since the 2D simulations were for replication purposes only it was deemed that a single sampling of the pressure values would be adequate for assessing the performance of the replicated models. The initial values utilised for the boundary conditions were set as absolute pressures and determined by experimental data from Rahimi (2017), with a primary inlet pressure of 200 kPa, a secondary inlet pressure of 1.8 kPa, and an outlet pressure of 2.84 kPa. The flow temperature for all boundaries was set to 300 K as per Al-Rbaihat (2020), with the walls represented as adiabatic surfaces.

The solution method employed an implicit formulation with second order spatial discretisation and a second order implicit transient formulation. A Courant number of 1 was also used as per the Al-Rbaihat (2020) settings. Monitoring of the simulations used residual values of 1e-7 to ensure a high quality convergence was attained. Hybrid initialisation was used before the calculations were performed for 10,000 time steps with a time step size of 5e-6 seconds and 150 iterations per time step.

3.6 Results/Discussion

The initial simulations were executed using the geometry model with a nozzle throat separation of 0.6 mm and an ejector throat separation of 3.0 mm. Figure 3.3 shows a contour plot of the Mach number for the solution provided after 10,000 time steps with a time step size of 5e-6 seconds. The flow depicted in figure 3.3 shows the primary flow being accelerated to approximately Mach 1 at the nozzle throat to achieve choked flow, but then fails to expand through the diverging supersonic nozzle despite its initial velocity increase to approximately Mach 1.75 directly after the throat. The flow adheres to the lower surface of the nozzle diverging section as it continues at a velocity of approximately Mach 1.2. After passing the nozzle exit the flow quickly dissipates with no apparent

entrainment achieved. An inspection of the boundary mass flow rates values of 8.73 g/s, -35.23 g/s, and -14.72 g/s were calculated for the primary inlet, secondary inlets, and the outlet respectively. The negative value for the secondary inlets identifies reversed flow at these boundaries is present.

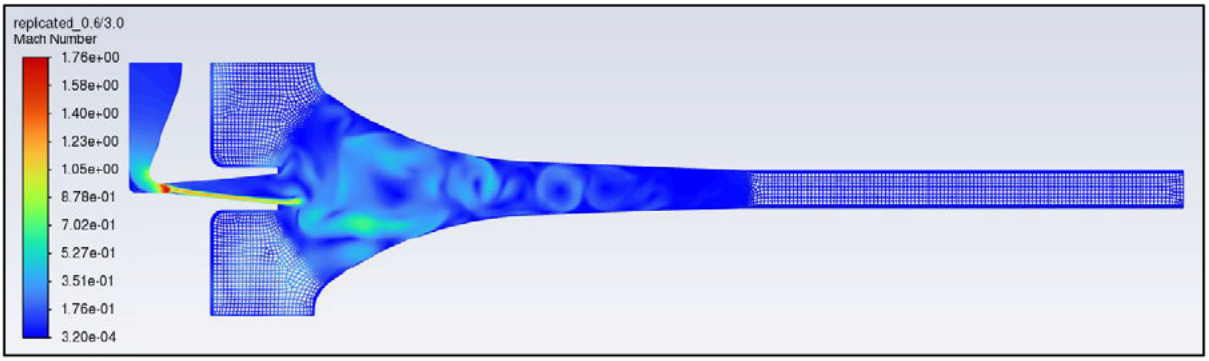

Figure 3.3: Mach number contour of replicated simulation.
(d = 0.6 mm, D = 3.0 mm, P_p = 200 kPa, P_s = 1.8 kPa, P_o = 2.84 kPa)

Due to early issues setting up simulations on the HPC, this simulation was performed on the personal laptop which gave a solution time of approximately 53 hours, as a consequence, constant monitoring of the simulation was not practical. Although the simulation ran to completion, the poorly represented flow depicted in figure 3.3, lead the author to believe that the residual criteria for convergence was not achieved for any time step during the simulation. As a means to check the model within a reasonable time frame it was decided to run the simulation as a steady flow scenario rather than transient, as was performed by Rahimi (2017) for the original VGRE.

Due to the fact that DES simulations are designed for 3D unsteady flow (Travin et al, 2000) a RANS SST k-ω turbulence model was selected to perform the steady flow simulation instead. All other simulation parameters remained consistent with the settings of the initial replicated simulation. Convergence was achieved after 778 iterations with the residuals set to 1e-7. Figure 3.4 shows the Mach number contour for the simulated solution, which depicts a much more reasonable representation of the flow behaviour through the improved VGRE with defined structures through the mixing section and flow directed straight towards the ejector's diffuser. The respective mass flow rates for the primary, secondary, and outlet flows were reported to be 5.76, 3.14, and -8.90 g/s. Using equation (2.1), the entrainment ratio (ω) was determined to be 0.55, providing a discrepancy of approximately 13% to Al-Rbaihat's (2020) experimental data. The results from the steady flow

simulation provided enough confidence in the geometry and mesh to proceed forward with the transient simulations again.

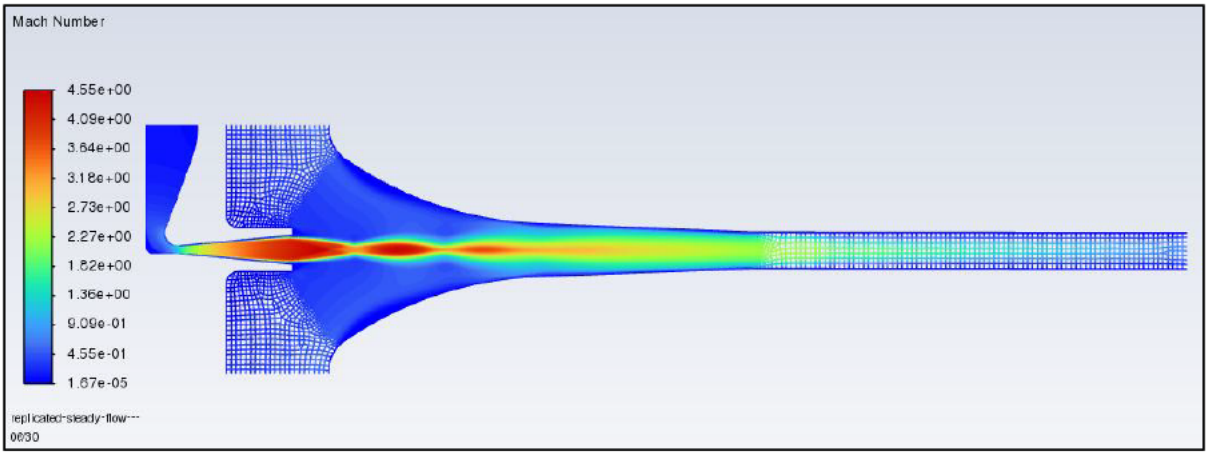

Figure 3.4: Mach number contour of steady flow replicated simulation.
(d = 0.6 mm, D = 3.0 mm, P_p = 200 kPa, P_s = 1.8 kPa, P_o = 2.84 kPa)

The subsequent simulation was conducted using a geometry configuration and boundary conditions that were well analysed by Al-Rbaihat (2020) to allow for better comparison. The geometry featured a nozzle throat separation of 0.6 mm and a duct throat separation of 2.3 mm and was simulated for a primary pressure of 250 kPa, secondary pressure of 1.8 kPa, and outlet pressure of 4.3 kPa. In an attempt to achieve a more computationally efficient solution different time advancement parameters were selected, these included a reduced time step size of 5e-8 seconds for a total of 10000 time steps, with a maximum of 50 iterations per time step. Figure 3.5 shows the Mach number contour provided by the solution, in which flow behaviour similar to figure 3.3 is observed. Again the choked condition of Mach 1 at the throat is achieved, followed by some flow expansion up to approximately Mach 2.4. The flow continues along the lower diverging section wall until flow separation occurs and eddys can be seen leaving the nozzle exit and continuing towards the outlet. The mass flow rates given by the simulation were 9.98 g/s, 49.44 g/s, and -59.94 g/s for the respective primary inlet, secondary inlets, and outlet. This equated to an entrainment ratio of 4.95, with a 1200% discrepancy from the experimental entrainment ratio of 0.38. In spite of efforts to produce simulations capable of better comparison, the replicated simulation offered negligible agreement to the experimental data and was determined to be a failed simulation.

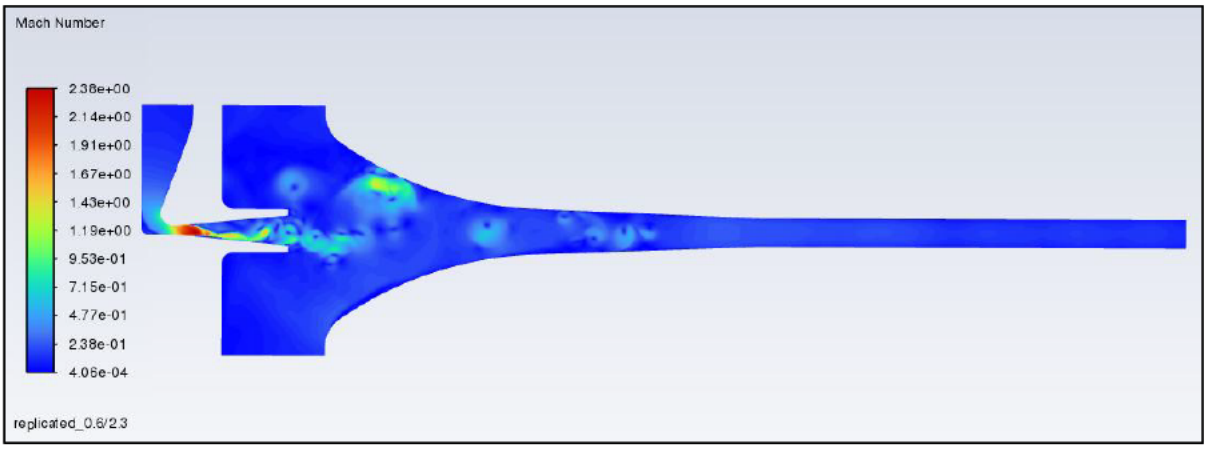

Figure 3.5: Mach number contour of replicated simulation.
(d = 0.6 mm, D = 2.3 mm, P_p = 250 kPa, P_s = 1.8 kPa, P_o = 4.3 kPa)

As a consequence of poor simulation results and ongoing difficulties to rectify their shortcomings, a sample of the improved VGRE simulations was acquired from Dr Raed Al-Rbaihat to assist in identifying a solution, this sample is referred to as the Al-Rb model. A comparison of the replicated and Al-Rb model geometries was conducted with some minor dimensional variations found, table 3.3 outlines the identified dimensions and their variance.

Table 3.3: Comparison of ejector geometry dimensions.

Dimensional Parameter	Al-Rb Model	Replicated Model	Variance (%)
Nozzle throat separation	0.49 mm	0.5 mm	2.04
Mixing section entrance separation	20 mm	19.987 mm	0.065
Primary nozzle converging half angle	21.989°	20.392°	7.26
Primary nozzle diverging half angle	5.1412°	5.4119°	5.27
Duct dimension - angle where converging/constant separation sections meet	177.71°	178°	0.16
Duct dimension - R3 arc length	3.0937 mm	3.1416 mm	1.55
Duct dimension - R30 arc length	17.135 mm	17.116 mm	0.11

The main variance between the drawings was determined to be both the converging and diverging half angles of the primary nozzle. The converging section is directly below the primary inlet and reduces the primary inlet cross-sectional area down before turning 90° to the nozzle throat. It is

uncertain if this variance would affect the flow after passing through the nozzle throat, however, as the simulations show an approximate Mach number of 1 at the nozzle throat this variance was deemed negligible. Whilst the nozzle diverging half angle does vary by approximately 5%, the angle of the replicated geometry falls within the optimal range as noted by Fu et al. (2016) of 10-12° for the full cone angle. All other dimensional variances were considered negligible and the replicated geometries were kept the same for the ongoing work.

Some differences were found in the meshing procedures employ for the replicated and AL-Rb model geometries, and as such revisions were made to the replicate the mesh to better reflect the Al-Rb model. The main element size was changed to 4e-4 m with a defeature size of 4e-5 m, and the inflation was defined by a first layer thickness of 4.4e-6 m with a total of 3 layers. The refined region element size was not adjusted. The mesh element counts produced by the revision presented a maximum variance of approximately 0.5% from the original values and were all still within the element range defined by Al-Rbaihat (2020). A comparison of the Al-Rb model and the equivalent replicated model, before and after revision, was performed to assess the quality of each mesh, shown in table 3.4.

Table 3.4: Mesh quality comparison values.

	Al-Rb Model			**Initial Model**			**Revised Model**		
Quality Metric	**Min**	**Max**	**Avg**	**Min**	**Max**	**Avg**	**Min**	**Max**	**Avg**
Orthogonality	0.523	1	0.994	0.498	1	0.994	0.508	1	0.994
Skewness	1.31e-10	0.635	4.5e2-2	1.31e-10	0.664	4.55e-2	1.31e-10	0.820	4.33e-2
Aspect Ratio	1	93.76	2.586	1	6.382	1.360	1	109.4	2.585

The mesh quality comparison shows that all meshes have very similar orthogonality values of with minimums of approximately 0.52, 0.50 and 0.51 for the Al-Rb, initial, and revised models respectively. The revised model compares poorly to the others, with regards to the maximum skewness at 0.82 versus 0.64 and 0.66 for the Al-Rb and initial models respectively. The initial model provided excellent maximum aspect ratio values compared to Al-Rb and the revised model, with respective values of 6.38, 93.76, and 109.4. Overall the best mesh was provided by the initial replicated model, however, because the aim was to replicate the Al-Rbaihat (2020) simulations it was decided to adopt the revised model meshes for all subsequent 2D simulations as they held better agreement to the Al-Rb model.

The Al-Rb model also defined a set of boundary conditions which could be utilised in model comparisons. These values were, 200 kPa at the primary inlet, 1.8 kPa at the secondary inlets, and 3.0 kPa at the outlet.

The operational issues with the HPC were resolved by this point in the project and so it was utilised to conduct all simulations moving forward. The next three subsequent simulations applied slight variations in an attempt to resolve the shortcomings of the previous non-converged replicated simulations. Each simulation used the same geometry with a nozzle throat separation of 0.6 mm and a duct throat separation of 3.0 mm. Table 3.5 lists the varied parameters for the three simulations.

Table 3.5: Replicated simulation parameters.

Parameter	**1st Simulation**	**2nd Simulation**	**3rd Simulation**
Primary pressure (P_p)	200 kPa	200 kPa	200 kPa
Secondary pressure (P_s)	1.8 kPa	1.8 kPa	1.8 kPa
Outlet pressure (P_o)	4.86 kPa	3.0 kPa	3.0 kPa
# Secondary inlet boundaries	1	2	2
Time step size	5e-6 sec	5e-6 sec	1e-7 sec
Number of time steps	10000	10000	10000
Max iterations/time step	150	150	150

Simulation 1 used the critical outlet pressure for the geometry configuration determined by the Al-Rbaihat (2020) experiments for the outlet pressure value. Simulation 1, along with all previous replicated simulations, were modelled with a single secondary boundary condition for both inlet sections. However, in conformity with the Al-Rb model settings, all succeeding replicated simulations employed two separate boundaries with the same condition settings. Simulation 2 was a direct replication of the Al-Rb model settings, and simulation 3 refined the time step size in an attempt to reach convergence. All three simulations presented with similar results to the previous replicated simulations as shown by the Mach number contours in figures 3.6, 3.7, and 3.8. The recorded mass flow rates and entrainment ratios are also given in table 3.6, however, as with the previous simulations these values are only representative of non-converged solutions.

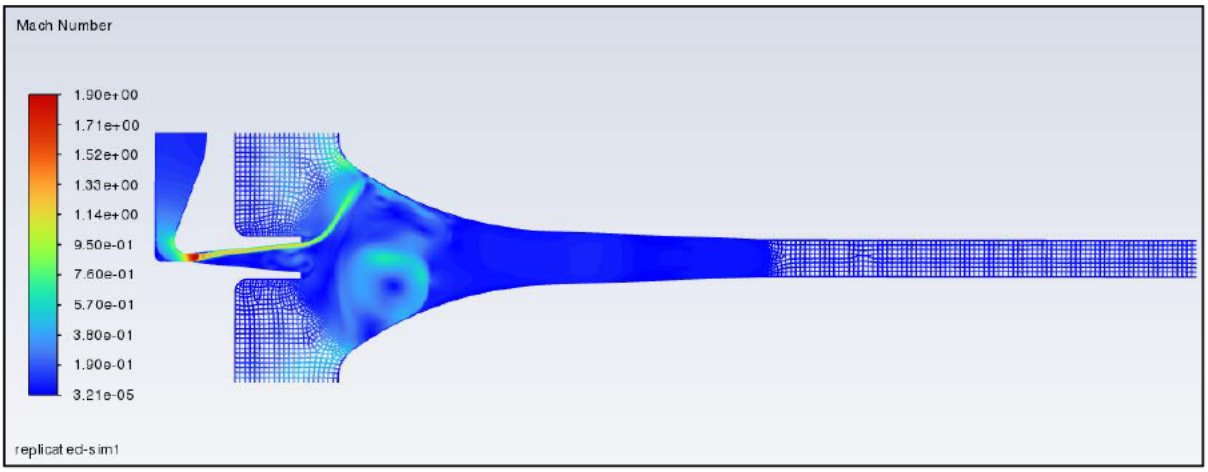

Figure 3.6: Mach number contour of 1st HPC replicated simulation.

(d = 0.6 mm, D = 3.0 mm, P_p = 200 kPa, P_s = 1.8 kPa, P_o = 4.86 kPa)

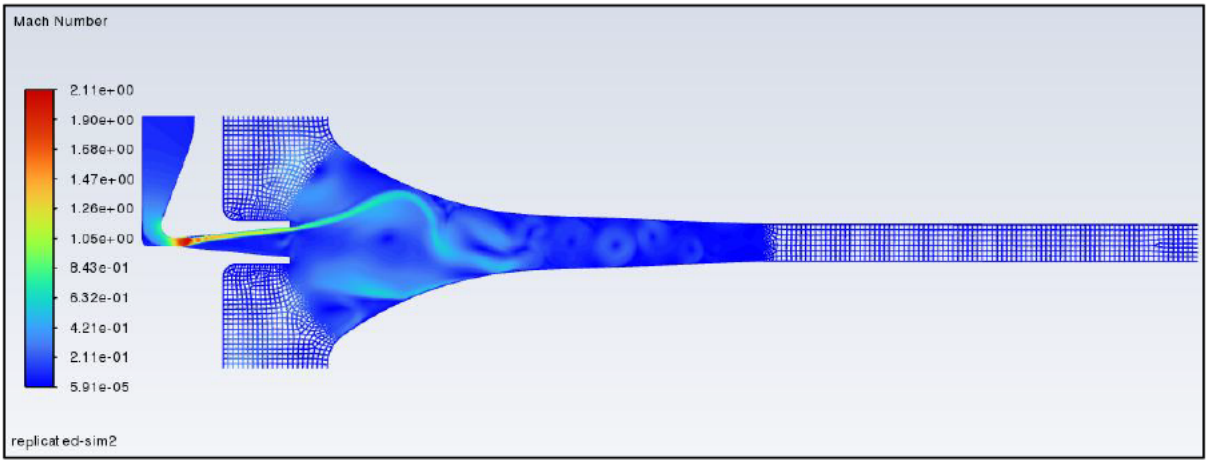

Figure 3.7: Mach number contour of 2nd HPC replicated simulation.

(d = 0.6 mm, D = 3.0 mm, P_p = 200 kPa, P_s = 1.8 kPa, P_o = 3.0 kPa)

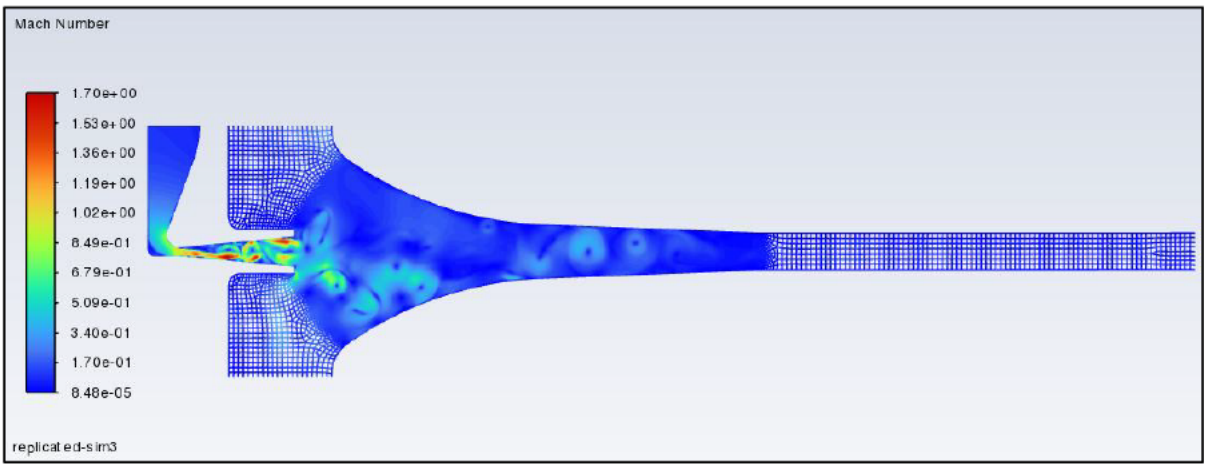

Figure 3.8: Mach number contour of 3rd HPC replicated simulation with reduced time step size.

(d = 0.6 mm, D = 3.0 mm, P_p = 200 kPa, P_s = 1.8 kPa, P_o = 3.0 kPa)

Table 3.6: Reported mass flow rates and entrainment ratios for replicated simulations.

	1st Simulation	2nd Simulation	3rd Simulation
Primary mass flow rate (g/s)	8.71	8.71	8.72
Secondary mass flow rate 1 (g/s)	-	24.24	36.52
Secondary mass flow rate 2 (g/s)	-	-14.06	6.45
Total Secondary mass flow rate (g/s)	-43.72	10.18	42.97
Outlet mass flow rate (g/s)	32.04	17.72	-18.35
Entrainment ratio	-5.02	1.17	4.93

A change of model was adopted to match the geometry configuration of the Al-Rb model, nozzle throat separation of 0.5 mm and duct throat separation of 2.6 mm. This was done as a means to produce a simulation with as little variance as possible to a known working model to achieve a converged solution.

Figure 3.9 shows the flow behaviour through the improved VGRE as simulated by the Al-Rb model, with shock structures extending from the fully expanded flow at the nozzle exit to the start of the ejector diffuser section. Conversely, Figure 3.10 shows an almost identical flow behaviour to the first replicated simulation, revealing another poor solution. The corresponding mass flow rate and entrainment ratio values are given in table 3.7 for the Al-Rb and equivalent replicated model simulations. Despite the poorly simulated flow behaviour, the equivalent replicated model provided an entrainment ratio of 0.39. This sits within the range of all entrainment ratio values determined by the experimental data (Al-Rbaihat, 2020), however, compared to the value of the Al-Rb model simulation it is approximately 26% lower.

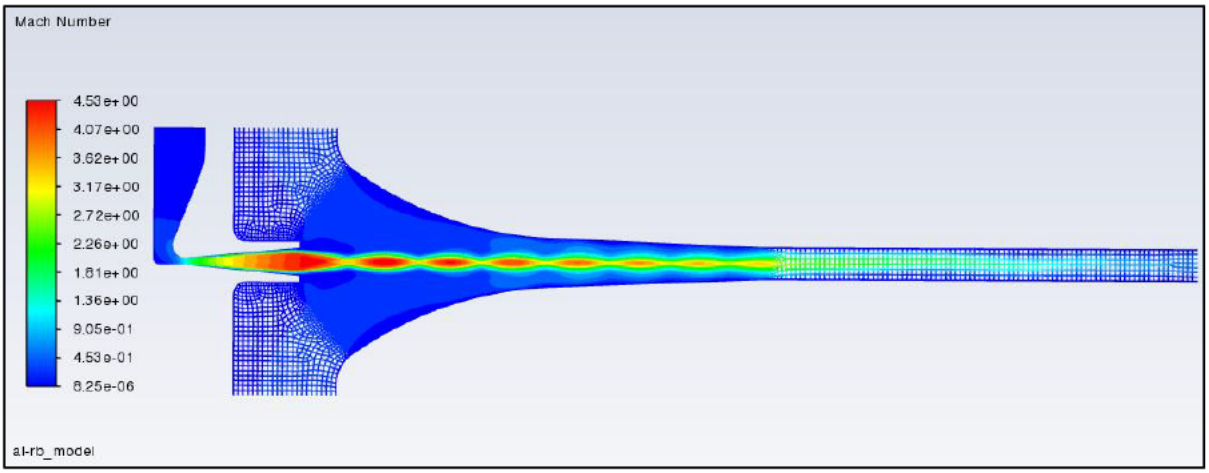

Figure 3.9: Mach number contour of Al-Rb model simulation.
(d = 0.5 mm, D = 2.6 mm, P_p = 200 kPa, P_s = 1.8 kPa, P_o = 3.0 kPa)

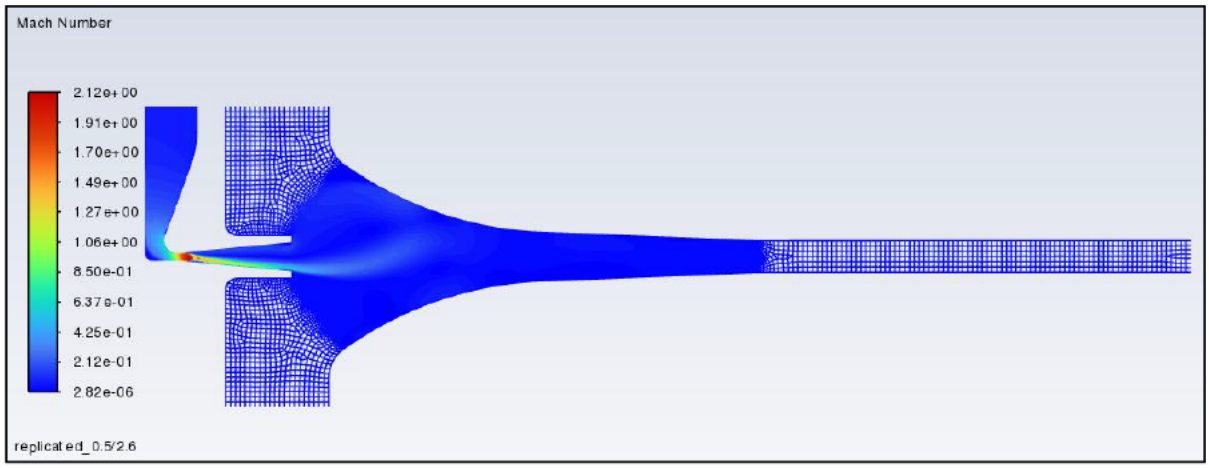

Figure 3.10: Mach number contour of replicated simulation.

(d = 0.5 mm, D = 2.6 mm, P_p = 200 kPa, P_s = 1.8 kPa, P_o = 3.0 kPa)

Table 3.7: Reported mass flow rates and entrainment ratios for Al-Rb and equivalent replicated model.

Parameter	Al-Rb Model	Equivalent Replicated Model
Primary mass flow rate (g/s)	4.76	7.32
Secondary mass flow rate 1 (g/s)	1.25	-4.83
Secondary mass flow rate 2 (g/s)	1..25	7.71
Total Secondary mass flow rate (g/s)	2.50	2.89
Outlet mass flow rate (g/s)	-7.25	-10.59
Entrainment ratio	0.53	0.39

3.7 Conclusions

The 2D simulations presented in this section represent the majority of the efforts applied in attempting to replicate the work performed by Al-Rbaihat (2020). The purpose of this task was to gain better personal understanding of the improved VGRE and its flow characteristics so that a suitable 3D model could be developed with confidence.

Other minor investigations, not detailed in this report, were also performed throughout the process of replicating the 2D simulations to determine which parameters should be simulated at full length. This was done as a result of unexpectedly long computational times that were unforeseen at the commencement of the project. The minor studies were performed by changing simulation variables and constantly monitoring the behaviour of the simulations through residual and other reporting

plots for a period of several hours. Common features in the plots (i.e. residuals not converging, irrational mass flow rate values) were continuously observed, determining the solutions not variable dependent. The simulation variables consisted mainly of solution method options, such as warped-face gradient correction, high order term relaxation, and high speed numerics.

Unfortunately, due to time constraints further investigation into the 2D simulation replications could not be continued. Instead it was decided to proceed with development of the 3D geometry and meshing so that some 3D DES simulations could be performed before the project deadline.

Chapter 4

3D Simulations

4.1 Chapter Overview

The shortcomings of the replicated 2D simulations meant that the original intended project objectives and methodology had been compromised. The inability to determine the cause of the poor solutions in the replicated simulations means that the accuracy of the replicated geometries and meshes could not be assessed before developing them into their 3D equivalents. However, in the process of performing the 2D simulations, a sample model from the improved VGRE simulations (referred to as the Al-Rb model), was acquired from Dr Raed Al-Rbaihat. This model was determined to have a reasonable level of agreement to experimental data when analysed by Al-Rbaihat (2020). Therefore, as a means to produce preliminary 3D simulations to assist further investigation in the future, the Al-Rb model was utilised in the development of the 3D geometry and mesh.

4.2 Geometry

The creation of the basic 3D geometric model, figure 4.1, was relatively straightforward. Using DesignModeler, the geometry was produced by revolving the 2D axisymmetric Al-Rb drawing, 360° around the axis of symmetry shown in figure 3.1. Several versions of the 3D geometry were adapted from this base model as a means to either implement a refinement region into the model or to provide a computationally efficient version for the meshing process.

The original intention for the meshing process was to implement the same element sizes to the 3D geometry as was used for the 2D axisymmetric simulations. For this reason, a 3D geometry was produced by revolving four separate sections of the improved VGRE, a primary nozzle/mixing section; two secondary inlet sections; and an outlet section. These regions, shown in figure 4.2,

were defined by the face splitting on the 2D geometry then revolved 360° around the axis of symmetry.

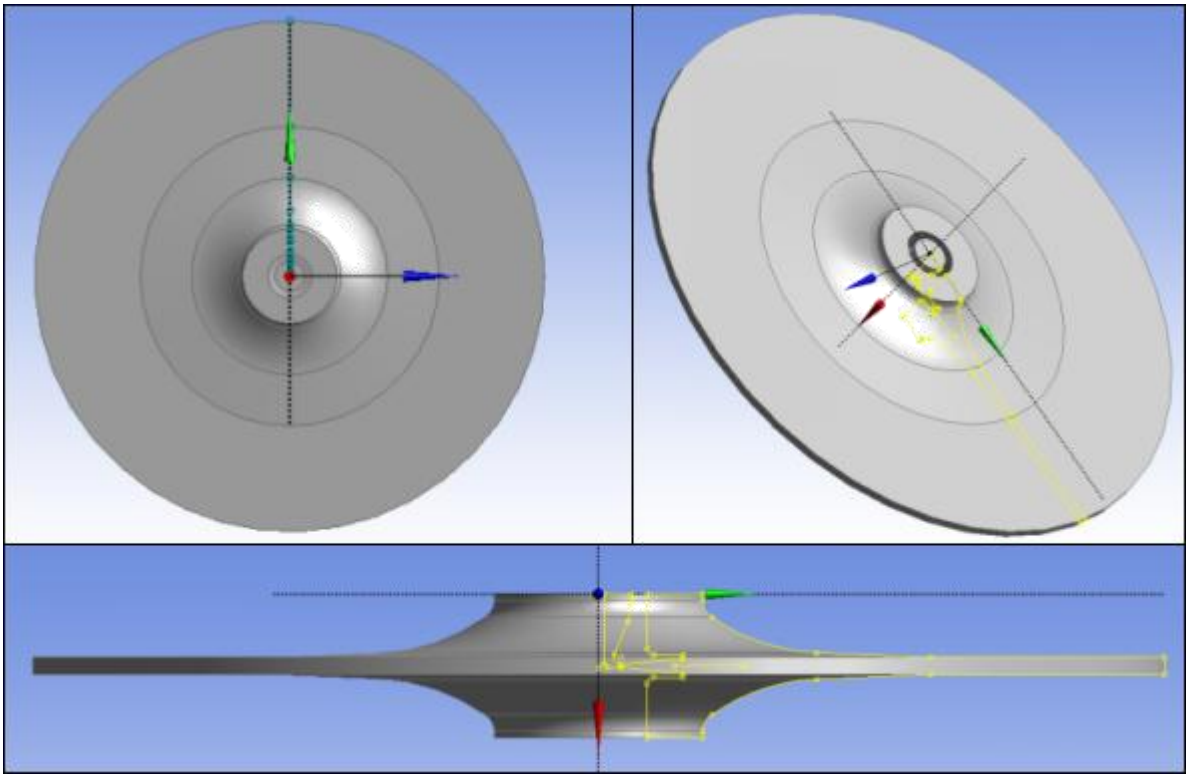

Figure 4.1: Images of the base 3D geometric model used in simulations.

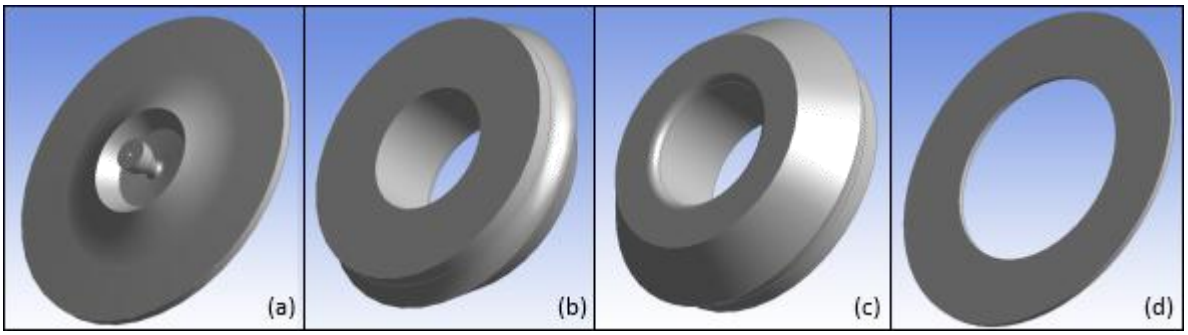

Figure 4.2: Revolved sections of improved VGRE 3D geometry variant.
(a) primary nozzle/mixing section, (b) secondary inlet 1 section, (c) secondary inlet 2 section, (d) outlet section.

Problems experienced during the meshing process, discussed in the next section, required additional geometry approaches to overcome. The result of which, saw the base geometry being divided into multiple, equally sized wedges. Originally being dissected into quarters, the geometry

was eventually revised to encompass eight 45° wedge sections as shown in figure 4.3. This geometry design was accomplished using the slice feature in DesignModeler to cut the model in the axial direction along four equally spaced, rotated planes.

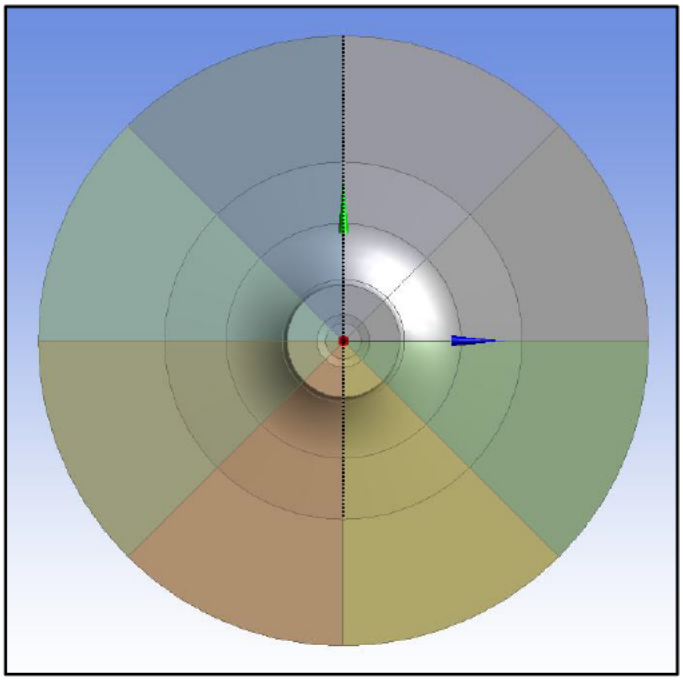

Figure 4.3: Geometric model with eight wedge sections.

4.3 Meshing

Meshing is a computationally heavy process, especially for 3D models. The meshing performed for the 3D simulations was primarily prepared on the personal laptop which, due to insufficient hardware specifications (16 Gb CPU memory/12 Gb GPU memory), placed limitations on the refinement of the meshes produced. Some attempts were made to perform meshing procedures on the HPC, however, this was not an efficient process so minimal meshes were produced this way.

As mentioned in section 4.2, the original intention for the meshing process was to implement the same element sizes to the 3D geometry as was used for the 2D axisymmetric simulations. To clarify, the face sizings for each of the four regions of the 2D geometry were to be translated to the maximum element size for each of the corresponding section volumes of the 3D geometry. However, the meshing program, ANSYS Mechanical, was not capable of performing this meshing approach and instead a sphere of influence was employed to produce a refined mesh. The sphere was

centered on the primary inlet with a radius of 3.5e-2 m, as shown in figure 4.4, this was large enough to refine the primary nozzle/mixing section and the two secondary inlets. An element size of 2e-4 m was achieved for the sphere of influence instead of the 6e-5 m used in the refined region of the 2D mesh. The remainder of the model outside the sphere was meshed with an element size of 8e-4 m, rather than 4e-4 m. Inflation was applied to all wall regions using the first layer thickness option set to 4.4e-6 m with three layers. These settings provided a mesh consisting of 13,344,658 cells. It should be noted that use of the sphere of influence makes the sectioned model redundant, but the sectioned geometry was still considered suitable for the purpose of the meshing process. Checking the quality metrics for the mesh determined a maximum skewness value of 0.799 and a minimum orthogonal quality value of 5.30e-2. Whilst the skewness may be considered acceptable, the minimum orthogonal quality is extremely low and could potentially cause the solution to diverge. These values are depicted in figure 4.5 by the chaotic and non-uniform mesh.

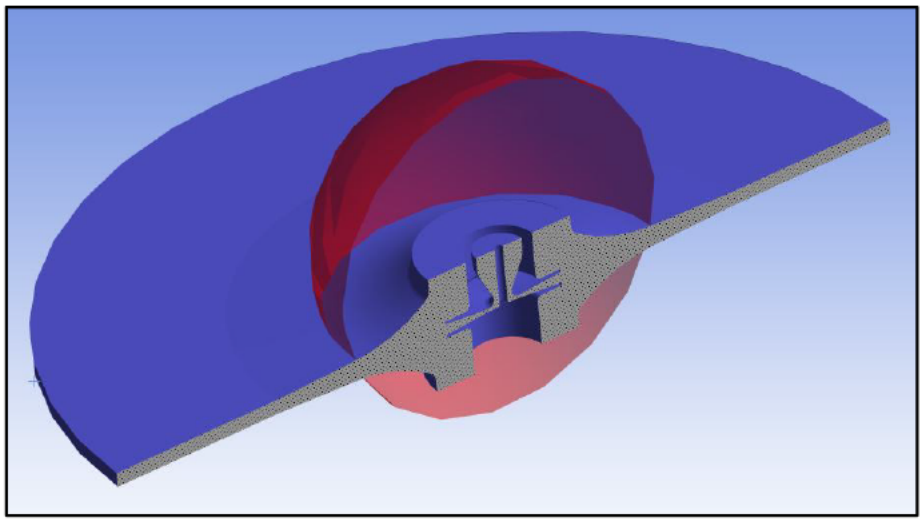

Figure 4.4: Sectioned image of improved VGRE with sphere of influence for refined meshing.

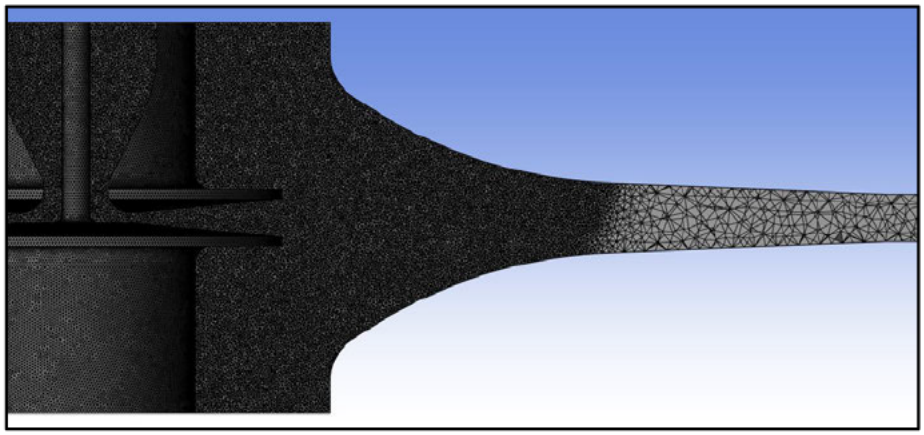

Figure 4.5: Sectioned view of mesh created using sphere of influence.

Further consideration was made with regards to the meshing approach, and a decision to investigate the sweep meshing approach as an alternative meshing solution was employed. Sweep meshing is a process where a face mesh is applied to one surface of the model and repeated incrementally along the length of the model to form the 3D mesh. This process works best with constant cross-sectional area models but can also be applied as a axisymmetrical sweep, revolving a cross-sectional face mesh around an axis. This method was used for the 3D model of the improved VGRE.

Figure 4.6 shows a sectioned view of the axisymmetric sweep mesh produced for the 3D model, which utilised a face element size of 4e-4 m, this measurement corresponds to the radial thickness of the elements. The arrangement of the cells is much more organised in this configuration providing a neater mesh with better quality than the sphere of influence model. The maximum skewness was reported to be 0.875 and the minimum orthogonal quality was 0.220, although better, these are still somewhat poor quality metric values. The face element size was also deemed considerably large compared to the 2D meshing refined region, however, this was a computational limit value.

To mitigate the large element sizing an approach was used whereby the 3D geometry was sliced, figure 4.3, into eight equally sized body segments. This had the effect of partitioning the model, allowing for less intensive computations. The personal laptop was able to create an axisymmetric sweep mesh with a face element size of 9e-5 m using this method, resulting in a total of 36,531,072 cells compared to 591,607 from the non-sliced geometry. The mesh quality also improved to a maximum skewness of 0.696 and a minimum orthogonal quality of 0.362. The two meshes can be compared in figures 4.6 and 4.7.

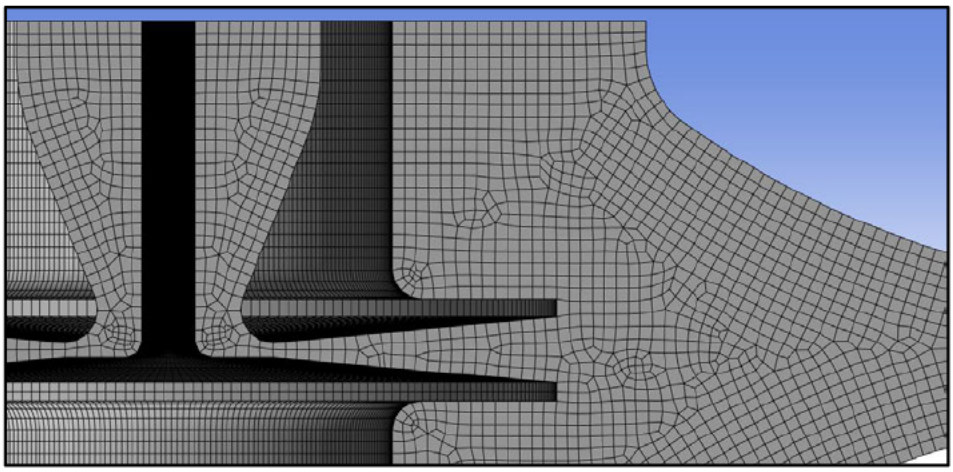

Figure 4.6: Axisymmetric sweep mesh with face element size of 4e-4 m.

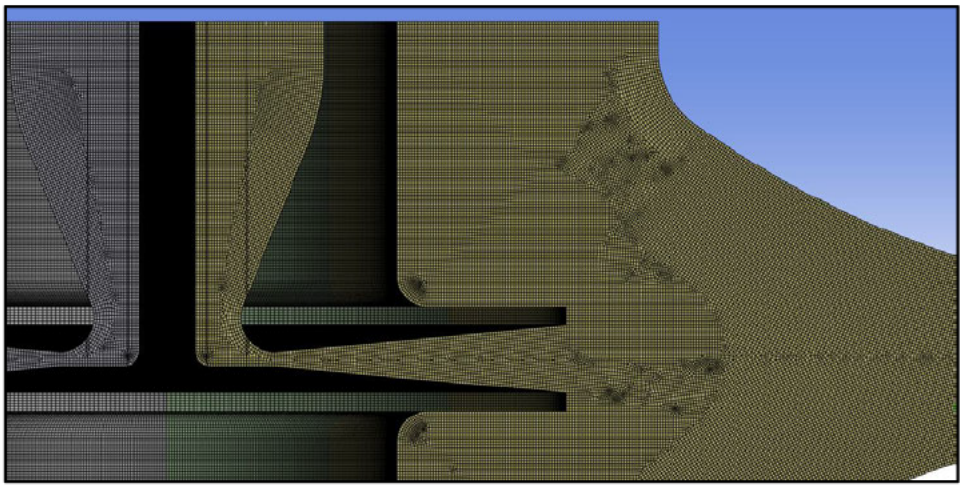

Figure 4.7: Axisymmetric sweep mesh with face element size of 9e-5 m.

The downside to using the sweep method was that inflation could not be implemented at the same time. The meshes created were all preliminary versions to gauge what was the best approach for future simulations. It should also be noted that all the meshes have capacity for refinement, particularly if processed on a mower powerful machine.

With project time restrictions being an issue, it was decided to perform a preliminary 3D simulation for the improved VGRE using a non-swept mesh with inflation layers equal to the 2D replicated simulations. The mesh was set with a face element size of 6.6e-4 m and a first layer thickness for the inflation of 4.4e-6 m, resulting in 2,598,355 cells. The mesh also utilised a feature in ANSYS Fluent which converts the tetrahedral volumes into polyhedral improving the quality of the mesh.

4.4 CFD Parameters

The parameters used for the 2D simulations were also adopted for the 3D simulations. A transient, density-based solver, using the DES SST k-ω turbulence model with the energy equation on. The boundary conditions matched the values from the Al-Rb model with a primary pressure of 200 kPa, a secondary pressure of 1.8 kPa, and an outlet pressure of 3.0 kPa. The working fluid was set to air as an ideal gas. The methods employed an implicit formulation with second order upwind spatial discretisation. The Courant number was also set to 1 to assist in managing the time step advancement. Residuals of 1e-4 were used to determine the level of convergence. The hybrid initialisation method was used before running the simulation for 1000 time steps with a time step size of 1e-7 seconds and 100 maximum iterations per time step.

4.5 Results/Discussion

The 3D simulation was performed using ANSYS Fluent 2023R1 on the HPC. All simulation settings matched the parameters of the 2D replicated simulations. With the poor simulations results produced for the 2D geometries, it was not certain how well the 3D simulations would perform. However, by using the same parameters the solution was able to produce similar results, shown in figure 4.8, identifying that the issue is in the parameters not the geometries.

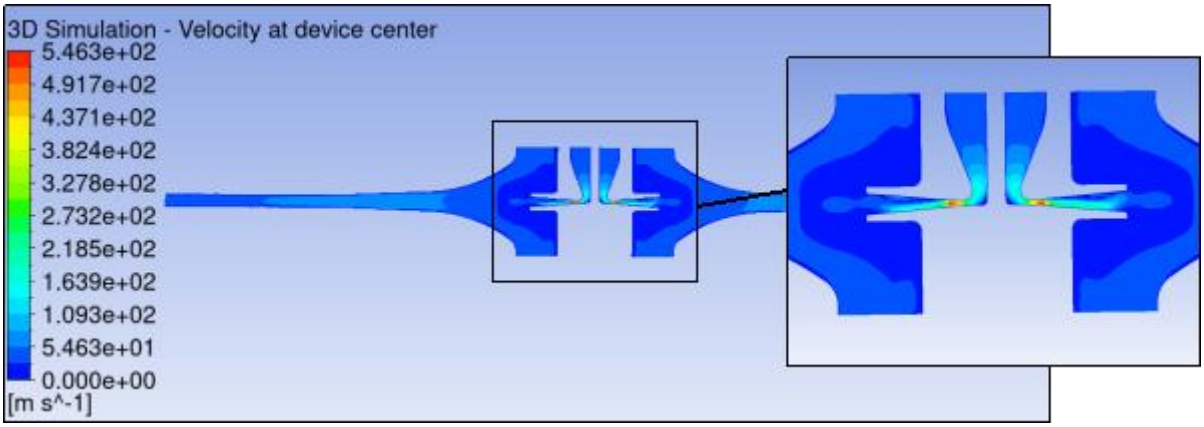

Figure 4.8: Flow velocity contour of preliminary improved VGRE 3D simulation.

The flow behaviour shown in figure 4.8 is similar to the flow simulated in the first 2D replicated simulation, shown in figure 3.3. Here the primary flow reaches approximately Mach 1 (343 m/s) at the throat for the choked flow, then accelerates briefly to approximately Mach 1.59 (546 m/s) before slowing to subsonic levels as it exits the nozzle diverging section. Figure 4.9 shows an isosurface plot for a velocity of Mach 1 situated in the throat of the nozzle, this is as viewed from the ejector outlet. Mass flow rate and entrainment ratios calculated from the simulation solution provided values of 9.4 g/s for the primary mass flow rate, 45.82 g/s for the secondary mass flow rate, -71.27 g/s for the outlet mass flow rate, and an entrainment ratio of 4.87.

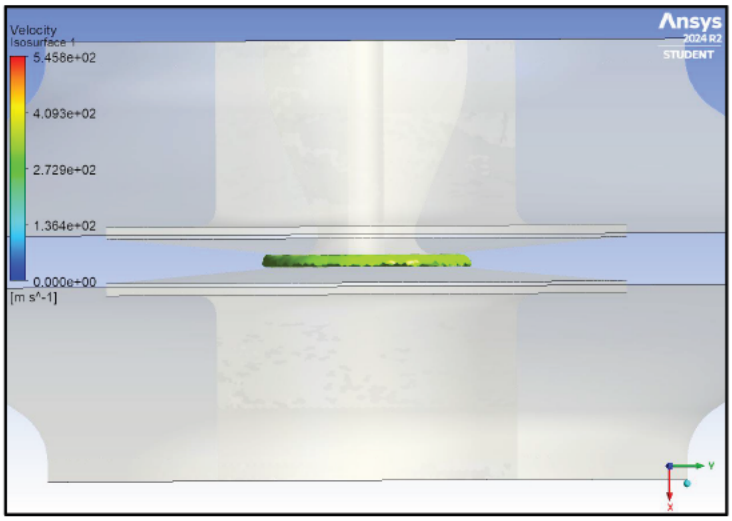

Figure 4.9: Isosurface plot of Mach 1 (343 m/s) velocity in nozzle throat.

Velocity streamline plots were also obtained showing the flow behaviour from a more 3 dimensional perspective. Figures 4.10(a) and 4.10(b) show the primary stream and figures 4.11(a) and 4.11(b) show the secondary stream behaviour. Once proper simulation parameters can be ascertained the streamline plots should offer some interesting insight into the simulated flow, and potentially identify new areas of the VGRE that can be improved.

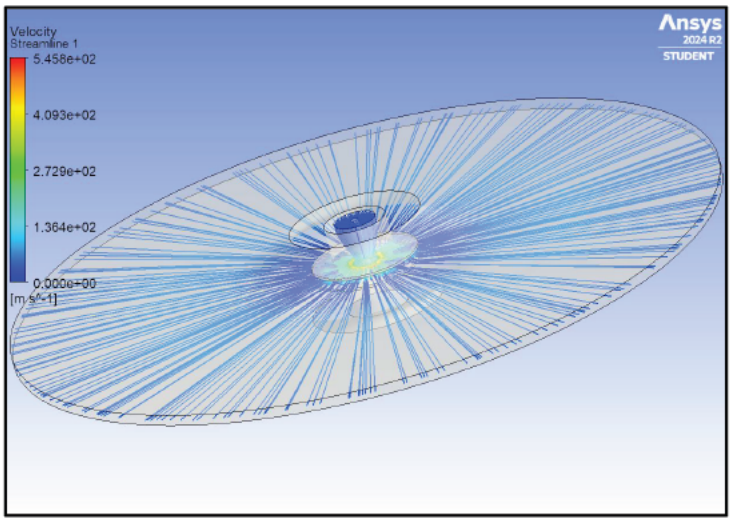

Figure 4.10(a): Velocity streamline plot of primary flow.

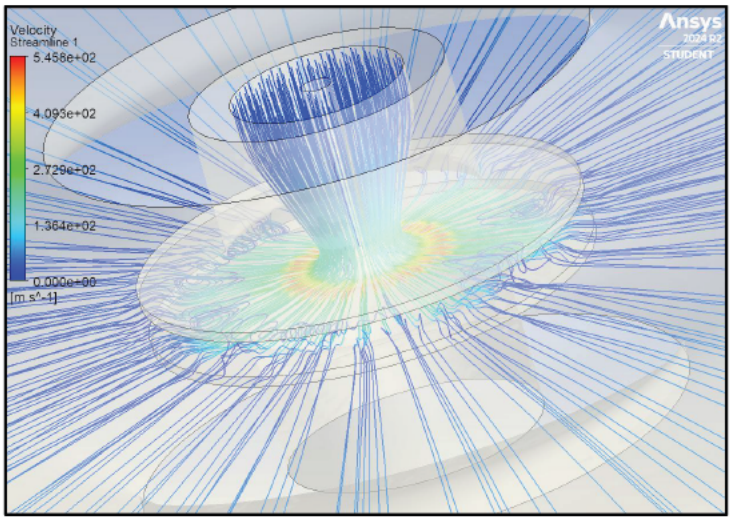

Figure 4.10(b): Velocity streamline plot of primary flow (zoomed).

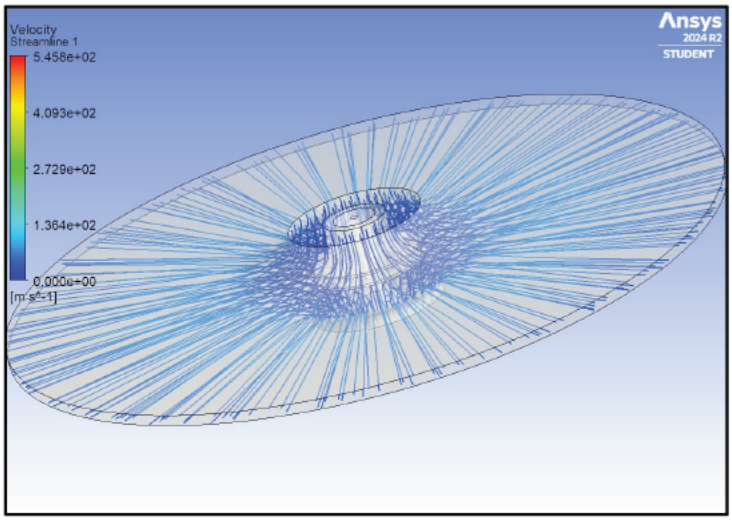

Figure 4.11(a): Velocity streamline plot of primary flow.

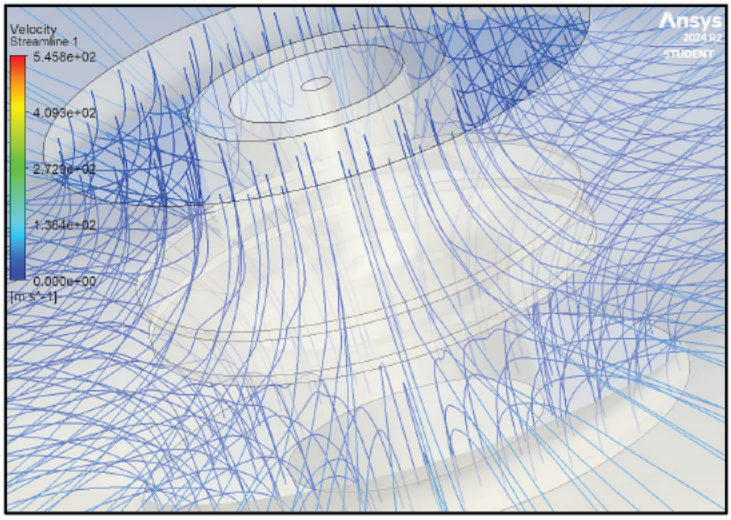

Figure 4.11(b): Velocity streamline plot of primary flow (zoomed).

4.6 Conclusions

Unfortunately the 3D simulation provided no better agreement to the experimental data collect by Al-Rbaihat (2020) than the 2D replicated simulations. It was determined, however, that the unidentified parameter was not a geometric factor and must therefore remain within the CFD settings. Due to project time constraints and deadlines, further 3D simulations could not be performed for the purpose of further investigation, and as such it was determined that the project should be concluded.

Chapter 5

Project Conclusions

5.1 Objective Summary

The focus of this project was to develop a reliable 3D CFD model for the purpose of investigating the improved VGRE further in a cost effective manner. The objectives outlined at the beginning of this dissertation were set as achievable milestones to reach this final goal.

Through research and reviews of the literature and previous work pertaining to the improved VGRE, an understanding of the ejector's function and form was attained by the author. With performance being a function of both geometry and operating conditions, there were many relationships identified which offered insight into potential ways to improve the VGRE beyond its current capabilities. These insights highlighted the need for an accurate numerical model, since there are too many factors affect performance to rely on experimental investigation alone. The previous work conducted in the development of the improved VGRE has had varied results but after review of the studies it is this authors opinion that the improved VGRE does present a viable solution to the issue of ejector efficiency.

The 2D analyses that were to be performed as part of the project objectives were far from successful. Multiple simulations of varying geometry configurations and simulation parameters were performed to poor result. However, during the preparation of this dissertation a previously unknown parameter was identified as the cause of the poor simulations. It was this authors belief that the pressure values were being applied as stagnation/absolute pressures for the boundary conditions as per Al-Rbaihat's (2020) documented parameters. As a consequence of inexperience and oversight an additional parameter was identified for an operating conditions setting. This was set to atmospheric pressure (101325 Pa) by default. By the time the issue was identified it was far

too late to perform any additional simulations and as such it will be noted in the recommendations for future reference. An additional oversight was discovered during the preparation of this dissertation, which inevitably held no consequence. The use of the DES SST k-ω turbulence model was used for simulations as a result of its extensive use throughout both Rahimi's (2017) and Al-Rbaihat's (2020) work. However, as reported by Al-Rbaihat (2020), an inaccurate experimental apparatus was used by Rahimi resulting in erroneous results. Ultimately, Al-Rbaihat determined the best turbulence model for simulating the improved VGRE is actually the DES Realizable k-ϵ model.

Development of the 3D geometry and mesh was a relative straightforward process, except for difficulties due to computational inadequacies of the hardware being used. The radial configuration of the improved VGRE allowed for a simple one-step conversion from a 2D to 3D geometry by way of the revolve function. The mesh development process identified several potential meshing methods including, sphere of influence for the refined nozzle/mixing section; axisymmetric sweep to provide uniform mesh structures; and segmented models to allow for more efficient computations of finer meshes..

As with the 2D replicated simulations, the 3D simulations were marred by the operating conditions setting. The 3D analyses objective was also affected by time constraints and project deadlines. The unforeseen issues experienced during the 2D simulations along with lengthy simulation times meant that only one 3D simulation could be performed to completion. Although, whilst the result were inherently erroneous they did present with similarities to the 2D simulations.

The data analysis objective was the least attended to, understandably. With poor results all that could be assessed was their common flow characteristics. This objective is reliant on results, for which there was few.

In completing this dissertation the author is fulfilling the final objective of reporting and presenting. The documentation presented here is indicative of the work performed over the course of this project, and is intended to aid any future work pertaining to the improved VGRE.

5.2 Recommendations and Further Work

The work performed over the course of this project has given the author a wealth of experience and knowledge. Although, the simulations were unsuccessful there were several factors that should be shared to assist with future work concerned with developing the improved VGRE.

- Set the operating conditions to zero to ensure stagnation/absolute pressures are correct.
- The DES Realizable k-ϵ turbulence model has been identified to have the best agreement to experimental data (Al-Rbaihat 2020).
- Be aware of simulation computing times, the 2D replicated simulations typically ran for over 30 hr on the HPC before completion.
- A Courant number of 1 is used in the simulations though this may be unnecessarily low for a density-based implicit formulation.
- There has been little investigation into the geometry of the secondary inlet flow section, there may be a similar relationship to the mixing section converging angle of axial ejectors.

In addition to these points, the recommendations stated by Rahimi (2017) and Al-Rbaihat (2020) should also be reviewed.

References

Ababneh, AK, Garris, CA, Jawarneh, AM & Tlilan, H 2009, 'Investigation of the Mach number effects on fluid-to-fluid interaction in an unsteady ejector with a radial-flow diffuser', *Jordan Journal of Mechanical and Industrial Engineering*, vol. 3, no. 2, pp. 131–140.

Al-Doori, G 2013, 'Investigation of refrigeration system steam ejector performance through experiments and computational simulations', Thesis, University of Southern Queensland.

Al-Rbaihat, R 2020, 'Design of variable geometry radial ejector for HVAC purposes through experiments and simulation', Thesis, University of Southern Queensland.

Al-Rbaihat, R, Saleh, K, Malpress, R & Buttsworth, D 2023, 'Experimental investigation of a novel variable geometry radial ejector', *Applied Thermal Engineering*, vol. 233, Elsevier BV, pp. 121143–121143, viewed 15 October 2024, <https://www.sciencedirect.com/science/article/pii/S1359431123011729?via%3Dihub>.

Ali, A 2013, 'Solar cooling: experiences and lessons learned with two different systems.', in *2013 International Renewable and Sustainable Energy Conference (IRSEC)*, IEEE, pp. 153–160.

Allouche, Y, Bouden, C & Riffat, S 2012, 'A Solar-Driven Ejector Refrigeration System for Mediterranean Climate: Experience Improvement and New Results Performed', *Energy Procedia*, vol. 18, pp. 1115–1124.

Arun Kumar, R & Rajesh, G 2019, 'Effect of Geometric Configurations on the Starting Transients in Vacuum Ejector', *AIAA Journal*, vol. 57, no. 7, pp. 2905–2922.

Bartosiewicz, Y, Zine Aidoun, Philippe Desevaux & Yves Mercadier 2005, 'Numerical and experimental investigations on supersonic ejectors', *International Journal of Heat and Fluid Flow*, vol. 26, Elsevier BV, no. 1, pp. 56–70.

Beithou, N & Aybar, HS 2000, 'A mathematical model for steam-driven jet pump', *International Journal of Multiphase Flow*, vol. 26, no. 10, pp. 1609–1619.

Bellos, E & Tzivanidis, C 2017, 'Optimum design of a solar ejector refrigeration system for various operating scenarios', *Energy Conversion and Management*, vol. 154, pp. 11–24.

Besagni, G, Mereu, R & Inzoli, F 2016, 'Ejector refrigeration: A comprehensive review', *Renewable and Sustainable Energy Reviews*, vol. 53, pp. 373–407.

Chaiwongsa, P & Wongwises, S 2008, 'Experimental study on R-134a refrigeration system using a two-phase ejector as an expansion device', *Applied Thermal Engineering*, vol. 28, no. 5-6, pp. 467–477.

Chandra, VV & Ahmed, MR 2014, 'Experimental and computational studies on a steam jet refrigeration system with constant area and variable area ejectors', *Energy Conversion and Management*, vol. 79, pp. 377–386.

Chesi, A, Ferrara, G, Ferrari, L & Tarani, F 2013, 'Analysis of a solar assisted vapour compression cooling system', *Renewable Energy*, vol. 49, pp. 48–52.

Chong, D, Hu, M, Chen, W, Wang, J, Liu, J & Yan, J 2014, 'Experimental and numerical analysis of supersonic air ejector', *Applied Energy*, vol. 130, pp. 679–684.

Chong, D, Yan, J, Wu, G & Liu, J 2009, 'Structural optimization and experimental investigation of supersonic ejectors for boosting low pressure natural gas', *Applied Thermal Engineering*, vol. 29, no. 14-15, pp. 2799–2807.

Colle, S, Pereira, GS, Gutiérrez, HRV & Moragas, RE 2009, 'On the validity of a design method for a solar-assisted ejector cooling system', *Solar Energy*, vol. 83, no. 2, pp. 139–149.

Cooper, B 2020, 'CFD analysis of a primary nozzle vortex generator on steam ejector performance.', Dissertation, University of Southern Queensland, pp. 90–96.

Dennis, M & Garzoli, K 2011, 'Use of variable geometry ejector with cold store to achieve high solar fraction for solar cooling', *International Journal of Refrigeration*, vol. 34, no. 7, pp. 1626–1632.

Diaconu, BM 2012, 'Energy analysis of a solar-assisted ejector cycle air conditioning system with low temperature thermal energy storage', *Renewable Energy*, vol. 37, no. 1, pp. 266–276.

Elbel, S & Hrnjak, P 2008, 'Ejector refrigeration: An overview of historical and present developments with an emphasis on air-conditioning applications', in *Proceedings of International Refrigeration and Air Conditioning Conference*.

Elbel, S & Lawrence, N 2016, 'Review of recent developments in advanced ejector technology', *International Journal of Refrigeration*, vol. 62, pp. 1–18.

Fu, W, Li, Y, Liu, Z, Wu, H & Wu, T 2016, 'Numerical study for the influences of primary nozzle on steam ejector performance', *Applied Thermal Engineering*, vol. 106, pp. 1148–1156.

Han, Y, Wang Xiao-dong, Sun, H, Zhang, G, Guo, L & Tu, J 2019, 'CFD simulation on the boundary layer separation in the steam ejector and its influence on the pumping performance', *Energy*, vol. 167, Elsevier BV, pp. 469–483.

Hemidi, A, Henry, F, Leclaire, S, Seynhaeve, J-M & Bartosiewicz, Y 2009, 'CFD analysis of a supersonic air ejector. Part I: Experimental validation of single-phase and two-phase operation', *Applied Thermal Engineering*, vol. 29, no. 8-9, pp. 1523–1531.

Hosseini Araghi, A & Khiadani, M 2018, 'Experimental investigation and analysis of a new single-stage vacuum spray flash desalinator utilising a gas-liquid ejector', *Journal of Cleaner Production*, vol. 190, pp. 118–127.

Huang, BJ, Chang, JM, Petrenko, VA & Zhuk, KB 1998, 'A solar ejector cooling system using refrigerant R141b', *Solar Energy*, vol. 64, no. 4-6, pp. 223–226.

Huang, BJ, Petrenko, VA, Samofatov, IYa & Shchetinina, NA 2001, 'Collector selection for solar ejector cooling system', *Solar Energy*, vol. 71, no. 4, pp. 269–274.

Jafarian, A, Azizi, M & Forghani, P 2016, 'Experimental and numerical investigation of transient phenomena in vacuum ejectors', *Energy*, vol. 102, pp. 528–536.

Jeon, Y, Jung, J, Kim, D, Kim, S & Kim, Y 2017, 'Effects of ejector geometries on performance of ejector-expansion R410A air conditioner considering cooling seasonal performance factor', *Applied Energy*, vol. 205, pp. 761–768.

Ji, M, Utomo, T, Woo, JS, Lee, Y, Jeong, H & Chung, H 2010, 'CFD investigation on the flow structure inside thermo vapor compressor', *Energy*, vol. 35, Elsevier BV, no. 6, pp. 2694–2702.

Jia, Y & Wenjian, C 2012, 'Area ratio effects to the performance of air-cooled ejector refrigeration cycle with R134a refrigerant', *Energy Conversion and Management*, vol. 53, no. 1, pp. 240–246.

Joemann, M, Oezcan, T, Kauffeld, M & Pollerberg, C 2016, 'Process Steam and Chilled Water Production with CPC-collectors, Steam Jet Ejector Chiller and Latent Heat Storages', *Energy Procedia*, vol. 91, Elsevier BV, pp. 767–776.

Khattab, NM & Barakat, MH 2002, 'Modeling the design and performance characteristics of solar steam-jet cooling for comfort air conditioning', *Solar Energy*, vol. 73, no. 4, pp. 257–267.

Korres, CJ, Bardakas, EE & Koumoutsos, NG 1989, 'Performance analysis of a solar vapour thermal compression chiller', *International Journal of Energy Research*, vol. 13, no. 2, pp. 243–252.

Kouhikamali, R & Sharifi, N 2012, 'Experience of modification of thermo-compressors in multiple effects desalination plants in Assaluyeh in IRAN', *Applied Thermal Engineering*, vol. 40, pp. 174–180.

Kubacki, S & Dick, E 2010, 'Simulation of plane impinging jets with k–ω based hybrid RANS/LES models', *International Journal of Heat and Fluid Flow*, vol. 31, no. 5, pp. 862–878.

Kumar, V, Subbarao, PMV & Singhal, G 2019, 'Effect of nozzle exit position (NXP) on variable area mixing ejector', *SN Applied Sciences*, vol. 1, no. 11.

Lin, C, Cai, W, Li, Y, Yan, J, Hu, Y & Giridharan, K 2013, 'Numerical investigation of geometry parameters for pressure recovery of an adjustable ejector in multi-evaporator refrigeration system', *Applied Thermal Engineering*, vol. 61, no. 2, pp. 649–656.

Liu, J, Wang, L, Jia, L & Wang, X 2017, 'The influence of the area ratio on ejector efficiencies in the MED-TVC desalination system', *Desalination*, vol. 413, pp. 168–175.

Liu, J, Wang, L, Jia, L & Xue, H 2019, 'Thermodynamic analysis of the steam ejector for desalination applications', *Applied Thermal Engineering*, vol. 159, Elsevier BV, pp. 113883–113883.

Ng, TT & Otis, DR 1979, 'Experimental Investigation of a Variable Geometry, Radial Ejector', *Journal of Fluids Engineering*, vol. 101, no. 4, pp. 491–494.

Nguyen, VM, Riffat, SB & Doherty, PS 2001, 'Development of a solar-powered passive ejector cooling system', *Applied Thermal Engineering*, vol. 21, no. 2, pp. 157–168.

Niu, L & Zhang, X 2024, 'Study on energy-saving applications of vacuum ejectors across various operational demands', *Vacuum*, vol. 228, p. 113527.

Palacz, M, Smołka, J, Kuś, W, Fic, A, Buliński, Z, Nowak, AJ, Banasiak, K & Hafner, A 2016, 'CFD-based shape optimisation of a CO 2 two-phase ejector mixing section', *Applied Thermal Engineering*, vol. 95, Elsevier BV, pp. 62–69.

Park, BH, Lim, JH & Yoon, W 2008, 'Fluid dynamics in starting and terminating transients of zero-secondary flow ejector', *International Journal of Heat and Fluid Flow*, vol. 29, no. 1, pp. 327–339.

Poirier, M 2022, 'Influence of operating conditions on the optimal nozzle exit position for vapor ejector', *Applied Thermal Engineering*, vol. 210, p. 118377.

Pollerberg, C, Ali, A & Dötsch, C 2008, 'Experimental study on the performance of a solar driven steam jet ejector chiller', *Energy Conversion and Management*, vol. 49, no. 11, pp. 3318–3325.

Pollerberg, C, Ali, A & Dötsch, C 2009, 'Solar driven steam jet ejector chiller', *Applied thermal engineering*, vol. 29, Elsevier BV, no. 5-6, pp. 1245–1252.

Pridasawas, W & Lundqvist, P 2007, 'A year-round dynamic simulation of a solar-driven ejector refrigeration system with iso-butane as a refrigerant', *International Journal of Refrigeration*, vol. 30, no. 5, pp. 840–850.

Rahimi, H 2017, 'Investigation of radial flow ejector performance through experiments and computational simulations', Thesis, University of Southern Queensland.

Rahimi, H, Buttsworth, D & Malpress, R 2017, 'CFD Study of a Variable Flow Geometry Radial Ejector', *Proceedings of the ... International Conference on Fluid Flow, Heat and Mass Transfer*.

Rahimi, H, Malpress, R & Buttsworth, D 2016, 'Investigation of radial flow ejector concept through CFD analysis', in *Proceedings of 20th Australasian Fluid Mechanics Conference*.

Ramesh, AS & Sekhar, SJ 2018, 'Experimental and numerical investigations on the effect of suction chamber angle and nozzle exit position of a steam-jet ejector', *Energy*, vol. 164, pp. 1097–1113.

Rand, CP, Croquer, S, Poirier, M & Poncet, S 2022, 'Optimal nozzle exit position for a single-phase ejector (Experimental, numerical and thermodynamic modelling)', *International Journal of Refrigeration*, vol. 144, Elsevier BV, pp. 108–117.

Ruangtrakoon, N, Thongtip, T, Aphornratana, S & Sriveerakul, T 2013, 'CFD simulation on the effect of primary nozzle geometries for a steam ejector in refrigeration cycle', *International Journal of Thermal Sciences*, vol. 63, pp. 133–145.

Rusly, E, Aye, L, Charters, WWS & Ooi, A 2005, 'CFD analysis of ejector in a combined ejector cooling system', *International Journal of Refrigeration*, vol. 28, no. 7, pp. 1092–1101.

Shi, L, Zhao, G, Yang, Y, Gao, D, Qin, F, Wei, X & He, G 2019, 'Research progress on ejector mode of rocket-based combined-cycle engines', *Progress in Aerospace Sciences*, vol. 107, pp. 30–62.

Śmierciew, K, Gagan, J, Butrymowicz, D & Karwacki, J 2014, 'Experimental investigations of solar driven ejector air-conditioning system', *Energy and Buildings*, vol. 80, pp. 260–267.

Sokolov, M & Hershgal, D 1993, 'Optimal coupling and feasibility of a solar-powered year-round ejector air conditioner', *Solar Energy*, vol. 50, no. 6, pp. 507–516.

Thongtip, T & Aphornratana, S 2017, 'An experimental analysis of the impact of primary nozzle geometries on the ejector performance used in R141b ejector refrigerator', *Applied Thermal Engineering*, vol. 110, pp. 89–101.

Travin, A, Shur, M, Strelets, M & Spalart, P 2000, 'Detached-eddy simulations past a circular cylinder', in *Flow, Turbulence and Combustion*, vol. 63, Kluwer Academic Publishers, Netherlands, pp. 293–313.

Utomo, T, Ji, M, Kim, P, Jeong, H & Chung, H 2008, 'CFD analysis on the influence of converging duct angle on the steam ejector performance.', paper presented at EngOpt , Rio de Janeiro, Brazil, pp. 2–8.

Van Nguyen, V, Varga, S, Soares, J, Dvorak, V & Oliveira, AC 2020, 'Applying a variable geometry ejector in a solar ejector refrigeration system', *International Journal of Refrigeration*, vol. 113, pp. 187–195.

Varga, S, Oliveira, AC & Diaconu, B 2009, 'Analysis of a solar-assisted ejector cooling system for air conditioning', *International Journal of Low-Carbon Technologies*, vol. 4, no. 1, pp. 2–8.

Vidal, H, Colle, S & Pereira, G dos S 2006, 'Modelling and hourly simulation of a solar ejector cooling system', *Applied Thermal Engineering*, vol. 26, no. 7, pp. 663–672.

Wang, L, Liu, J, Zou, T, Du, J & Jia, F 2018, 'Auto-tuning ejector for refrigeration system', *Energy*, vol. 161, Elsevier BV, pp. 536–543.

Wongwises, S & Disawas, S 2005, 'Performance of the two-phase ejector expansion refrigeration cycle', *International Journal of Heat and Mass Transfer*, vol. 48, no. 19-20, pp. 4282–4286.

Wu, H, Liu, Z, Han, B & Li, Y 2014, 'Numerical investigation of the influences of mixing chamber geometries on steam ejector performance', *Desalination*, vol. 353, pp. 15–20.

Wu, Y, Zhao, H, Zhang, C-Q, Wang, L & Han, J 2018, 'Optimization analysis of structure parameters of steam ejector based on CFD and orthogonal test', *Energy*, vol. 151, pp. 79–93.

Yadav, SK, Murari Pandey, K & Gupta, R 2021, 'Recent advances on principles of working of ejectors: A review', *Materials Today: Proceedings*, vol. 45, pp. 6298–6305.

Yu, M, Zou, L & Yu, J 2024, 'Numerical investigation on the effect of area ratio on an adjustable ejector for heat pump dryer based on dynamic mesh', *Energy*, vol. 308, p. 132876.

Zhou, L, Zhao, R & Yuan, W 2018, 'An investigation of interface conditions inherent in detached-eddy simulation methods', *Aerospace Science and Technology*, vol. 74, Elsevier BV, pp. 46–55.

Zhu, Y, Cai, W, Wen, C & Li, Y 2009, 'Numerical investigation of geometry parameters for design of high performance ejectors', *Applied Thermal Engineering*, vol. 29, no. 5-6, pp. 898–905.

Zhu, Y & Jiang, P 2014, 'Experimental and numerical investigation of the effect of shock wave characteristics on the ejector performance', *International Journal of Refrigeration*, vol. 40, pp. 31–42.

Appendix

Project Specification

ENP4111 Professional Engineering Research Project

Project Specification

For: **Lachlan Rae**
Topic: 3-Dimensional Detached Eddy Simulations of a Novel Variable Geometry Radial Ejector
Supervisors: Dr Khalid Saleh
Sponsorship: Faculty of Health, Engineering & Sciences
Project Aim: To develop a cost effective, accurate, and reliable 3D DES model for the purpose of performing numerical simulations and to assist in the development of a novel variable geometry radial ejector

Program:

1. Learn ANSYS software and familiarise with the fundamental concepts of the novel variable geometry radial ejector.

2. Reproduce 2D axisymmetric geometries and conduct simulations of previous novel variable geometry radial ejector studies, and verify the accuracy.

3. Conduct background research regarding the development of the novel variable geometry radial ejector and the geometric characteristics that influence its performance.

4. Develop 2D geometries into 3D variants and perform meshing application to provide a suitably refined mesh for simulating the novel variable geometry radial ejector

5. Perform 3D DES simulations for a range of variable geometry radial ejector geometry configurations

6. Analyse the result of the simulations, compare with the 2D simulation results, and use experimental data to validate the results

Resource requirements:

Item/Resource	Quantity	Cost	Source
ANSYS Student Software	1	Nil	Free download for students and available on university computers
ANSYS Tutorials and Users Guide	1	Nil	Available free online and from MEC5100 course material
Guidance of Project Supervisor	N/A	Nil	Dependent on the availability of the Supervisor
Time to Conduct the Research	N/A	Nil	Research will likely require all of the allocated time
Internet Access for Literature	1	Nil	University has unlimited WiFi
Unlimited Access to a Computer	1	Nil	Unlimited access to personal computer and university computers